

Article

Investigation of Convective and Radiative Heat Transfer of 21700 Lithium-Ion Battery Cells

Gábor Kovács, Szabolcs Kocsis Szürke  and Szabolcs Fischer * 

Central Campus Győr, Széchenyi István University, H-9026 Győr, Hungary; gabor.kovacs.oe@gmail.com (G.K.); kocsis.szabolcs@ga.sze.hu (S.K.S.)

* Correspondence: fischersz@sze.hu; Tel.: +36-(96)-503-400

Abstract

Due to their high energy density and power potential, 21700 lithium-ion battery cells are a widely used technology in hybrid and electric vehicles. Efficient thermal management is essential for maximizing the performance and capacity of Li-ion cells in both low- and high-temperature operating conditions. Optimizing thermal management systems remains critical, particularly for long-range and weight-sensitive applications. In these contexts, passive heat dissipation emerges as an ideal solution, offering effective thermal regulation with minimal additional system weight. This study aims to deepen the understanding of passive heat dissipation in 21700 battery cells and optimize their performance. Special emphasis is placed on analyzing heat transfer and the relative contributions of convective and radiative mechanisms under varying temperature and discharge conditions. Laboratory experiments were conducted under controlled environmental conditions at various discharge rates, ranging from $0.5 \times C$ to $5 \times C$. A 3D-printed polymer casing was applied to the cell to enhance thermal dissipation, designed specifically to increase radiative heat transfer while minimizing system weight and reliance on active cooling solutions. Additionally, a numerical model was developed and optimized using experimental data. This model simulates convective and radiative heat transfer mechanisms with minimal computational demand. The optimized numerical model is intended to facilitate further investigation of the cell envelope strategy at the module and battery pack levels in future studies.



Academic Editor: Leon L. Shaw

Received: 30 April 2025

Revised: 17 June 2025

Accepted: 18 June 2025

Published: 26 June 2025

Citation: Kovács, G.; Kocsis Szürke, S.; Fischer, S. Investigation of Convective and Radiative Heat Transfer of 21700 Lithium-Ion Battery Cells. *Batteries* **2025**, *11*, 246. <https://doi.org/10.3390/batteries11070246>

Copyright: © 2025 by the authors. Licensee MDPI, Basel, Switzerland. This article is an open access article distributed under the terms and conditions of the Creative Commons Attribution (CC BY) license (<https://creativecommons.org/licenses/by/4.0/>).

1. Introduction

Lithium-ion (Li-ion) batteries have become the dominant energy storage technology across a broad range of applications, from small handheld electronics to electric vehicles (EVs) and even unmanned aerial systems (UAS). Among the various form factors available, cylindrical cells—particularly the 18650 and 21700 formats—have gained widespread popularity due to their mechanical robustness, high energy density, and adaptability for modular integration [1,2]. In these designations, the first two digits represent the cell diameter in millimeters, the following two digits denote the height, and the final “0” indicates a cylindrical geometry. These compact cells can be readily scaled to meet high power demands by arranging them in series or parallel modules.

Despite their numerous advantages, Li-ion cells are thermally sensitive. At low temperatures, increased internal resistance leads to diminished usable capacity, while elevated temperatures accelerate degradation and pose safety risks, including thermal runaway [3].

However, operating cells within a moderate temperature range (~30–40 °C) can enhance Li-ion kinetics and reduce internal resistance, thus improving power performance. Electrochemical processes inherently generate heat during normal operation, whether charging or discharging. As power demands continue to rise, with trends toward fast charging and high discharge rates, thermal management becomes an essential aspect of battery system design. Thermal regulation safeguards against failure and maximizes performance and service life—a significant consideration given that battery systems often constitute a vehicle's most expensive component [4].

The 21700 cell format, with its higher energy density and larger capacity compared to 18650 cells, is increasingly favored in high-performance and weight-sensitive applications such as electric aviation and drone technologies. These use cases not only demand high power output for rapid maneuvers and altitude changes but also require lightweight designs to maximize payload and range. However, such conditions significantly increase heat generation. For instance, at a $5 \times C$ discharge rate (where C is the measurement of current at which a battery is charged and discharged, i.e., if the battery's capacity is 10 Ah, the $5 \times C$ equals $5 \times 10 = 50$ A/Amper/testing current during discharging), a 21700 cell can reach its thermal safety threshold of 85 °C in less than a minute without active cooling [5]. Therefore, effective and lightweight thermal management strategies are critical.

Traditional battery thermal management (BTM) systems typically rely on active cooling techniques, such as forced air or liquid circulation [6]. However, these systems add mass and complexity, which are highly undesirable in range-critical applications [7]. To address this challenge, passive thermal management approaches that require minimal additional weight have gained increasing attention. Such methods aim to optimize heat dissipation from the cell surface to the surrounding environment through natural convection and thermal radiation without the need for circulating fluids or heavy heat sinks.

The combined heat transfer from a cylindrical battery cell to its environment can be described by Equation (1) [8].

$$H_t^{out} = H_C + H_R = h \cdot A \cdot (T - T_a) + \sigma \cdot \varepsilon \cdot A \cdot \frac{1}{2} \left(T^4 - T_a^4 \right) \quad (1)$$

The mechanism of the heat transfer is H_t^{out} , where the first part (H_C) is related to the convective heat transfer, while the second part (H_R) corresponds to the radial heat transfer.

In the right part of Equation (1), h is the temperature-dependent heat transfer coefficient [$\text{W}/(\text{m}^2\text{K})$], A is the surface area of the cell [m^2], T and T_a are the cell temperature and the ambient temperature [K], $\sigma = 5.67 \times 10^{-8} [\text{W}/(\text{m}^2\text{K}^4)]$ is the Stefan–Boltzmann constant, and ε is the surface emissivity of the materials.

Examining Equation (1), it is clear that as the difference between the cell temperature (T) and the ambient temperature (T_a) increases, the radiative term becomes more dominant, as the temperature values in the radiative term are on the fourth power. In addition to the temperature values, the surface emissivity (ε) greatly influences the results. Thus, the different temperatures and surface emissivity should be monitored and carefully considered in thermal modeling and design.

Although many studies have focused on natural convection as the dominant passive cooling mechanism for cylindrical cells [9], a common method to simplify the ambient environment with a single heat flux on the surface of the cell [10], and relatively few have examined the contribution of thermal radiation in detail [11]. Nevertheless, radiative transfer can become dominant at elevated temperatures. For example, Shadman Rad et al. [8] experimentally demonstrated that at +40 °C, radiative heat transfer can exceed convective heat transfer ($H_R/H_C \sim 150\%$), whereas at lower temperatures, it contributes less than half ($H_R/H_C \sim 46\%$).

Other studies, such as that by Tan et al. [12], highlight the importance of surface emissivity. Their experiments showed that increasing the emissivity of cylindrical Li-ion cells significantly improves thermal radiation performance. They concluded that up to 50% of total heat dissipation could occur via radiation and recommended that battery designers consider emissive coatings or materials when selecting cell packaging.

Thermal modeling of Li-ion cells often requires simplifications to remain computationally tractable. These may include representing heat generation as volumetric sources or using surface-based “heat flux” boundary conditions [11,13]. While such approximations are adequate for many use cases, high-temperature applications require more accurate treatment of all heat transfer mechanisms, particularly radiation, which becomes increasingly important as temperature rises.

In the following paragraphs, the author of the current study collected the main results of the international literature on the related topic.

Liu et al. [14] present a comprehensive numerical study that validates models for predicting the thermal behavior of 21700 cylindrical batteries under multiple discharge rates. The experiments revealed effective correlations between the predicted and measured temperatures of the cells, highlighting how structured numerical models can be leveraged to simulate thermal performance accurately. This approach is instrumental for optimizing thermal designs and understanding the convective and radiative heat transfer dynamics prevalent in battery operations.

The implications of battery casing design become apparent in exploring radiative heat transfer. A 3D-printed polymer casing, as posited in the study, enhances radiative heat transfer, thereby augmenting the thermal management of the battery without adding considerable weight to the overall system [14]. The modeling frameworks outlined by Madani et al. further support this by detailing thermal behaviors and optimization techniques applicable to various designs of lithium-ion batteries [15], which can be essential when considering the skin factors of the battery casing.

Another vital aspect is to consider the operational environment of these batteries, particularly regarding their age, charge state, and outdoor conditions. Studies have reported varying thermal responses based on the state of charge (SOC), illustrating how aged batteries display altered thermal characteristics compared to newer cells [16]. Enhanced thermal management systems must, therefore, accommodate these variable states, including transient heating events during high discharge conditions, as identified by Du et al. [17]. These findings stress the need for adaptive thermal management approaches that respond dynamically to changing thermal loads.

The importance of model validation using experimental data cannot be overstated, as observed in studies that utilize multiple characterization techniques to analyze thermal behaviors. The research has indicated that the heat generation and performance of battery cells are notably impacted by the specific conditions under which they are tested, specifically noting the varying charge states and their consequent thermal behaviors [18]. Such insights underscore the importance of experimentally validated models for accurate predictions of thermal stability and operational safety.

The interplay between different discharging conditions and subsequent heat dissipation mechanisms has also been scrutinized. Recent studies have shown that higher discharge rates (e.g., above $1 \times C$) significantly raise the internal temperatures of the cells, necessitating enhanced cooling and thermal regulation strategies [19]. As indicated, batteries operating at high rates may require combined heat transfer mechanisms that incorporate both convective and radiative cooling methods to maintain optimal performance.

Moreover, the reliability of cooling systems is crucial as it directly impacts the lifespan and safety of battery cells. Along these lines, advancements in thermal management

systems, such as incorporating phase change materials (PCMs), have improved temperature uniformity across battery modules, thus enhancing overall thermal performance and cycling stability [20]. These materials, known for their heat absorption and release capabilities, provide a promising avenue for passive thermal management, alleviating the dependency on bulky and heavy active cooling systems [21].

Additionally, computational fluid dynamics (CFD) simulations are increasingly employed to examine the heat dissipation performance of lithium-ion battery packs under diverse configurations and operating scenarios. Models developed by Zhao et al. [22] demonstrate how different cooling pathways can profoundly influence the thermal profiles within battery packs. This predictive capability highlights the potential for engineering solutions that maximize heat dissipation while minimizing weight, an essential criterion for applications in electric vehicles.

Safety considerations surrounding thermal runaway also warrant attention in this context. Studies have comprehensively documented the triggering conditions for thermal runaway, emphasizing the critical thermal thresholds, hovering around 127 °C to 128 °C, above which batteries can undergo catastrophic failure [23]. Thus, ensuring that thermal management systems effectively maintain operational temperatures below this critical threshold is vital for safety.

The thermal behavior of lithium-ion batteries, particularly under varying discharge rates and configurations, reveals a complex interplay between thermodynamics, electrochemical performance, and safety parameters. Continued developments in numerical modeling, combined with empirical testing, will be essential in refining the understanding of these relationships and ultimately improving the designs of thermal management strategies for 21700 cells [24]. This integrative approach facilitates a more robust framework for addressing the challenges posed by thermal dynamics in lithium-ion batteries.

To encompass both convective and radiative heat transfer mechanisms in these batteries requires an understanding of not only the environmental conditions but also how different materials and configurations interact under operational loads. As research progresses, it becomes increasingly evident that multidimensional modeling approaches are crucial in accurately capturing such dynamics, thereby ensuring optimal design and application in real-world scenarios.

Furthermore, the implications of these studies extend beyond mere performance optimization; they speak to an overarching need for safety and reliability in battery storage technologies, which will be paramount as electric vehicle adoption accelerates. Through advanced thermodynamic modeling and a detailed grasp of the underlying physics, future investigations can aim to mitigate the risks associated with thermal runaway, thus paving the way for safer lithium-ion battery applications in everyday technologies.

The current study focuses on scenarios where structural weight constraints preclude using complex or heavy cooling systems. One such example is drone propulsion systems, where thermal regulation must be achieved without sacrificing payload capacity or flight time. The feasibility of enhancing passive radiative cooling through advanced surface treatments or structural materials is examined in this context.

To this end, the authors of the current study propose a lightweight, 3D-printed polymer casing designed to increase the surface emissivity of cylindrical cells. The selected polymers are compatible with modular integration and offer promising thermal properties. The study examines how this approach can improve passive cooling performance under high-discharge conditions without relying on active components.

To validate the concept, both experimental and numerical investigations were carried out. The experimental work included discharge tests across multiple current rates ($0.5 \times C$ to $5 \times C$) under controlled environmental conditions. The numerical simulations implemented

both convective and radiative heat transfer models optimized for experimental data (see Figure 1).

I. Battery Heat Generation Analysis

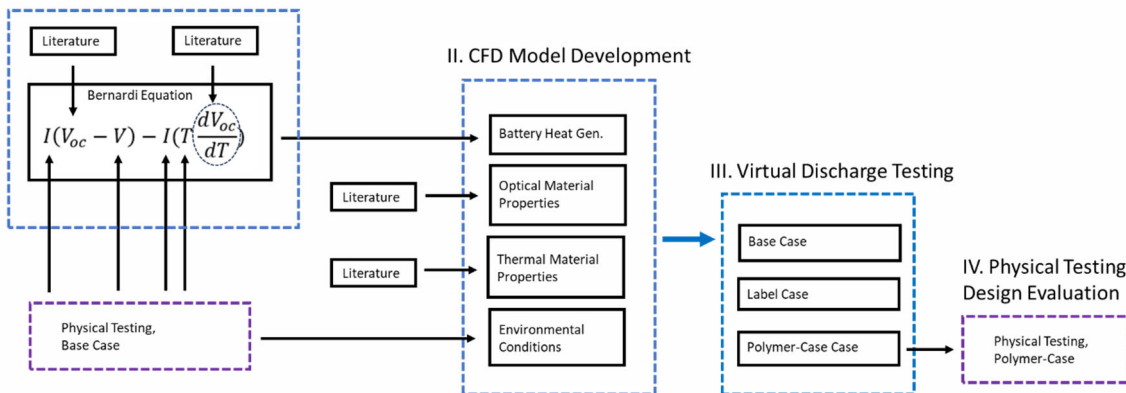


Figure 1. Showing the workflow diagram of the current study.

The following research questions are addressed in this paper:

- How much heat can be dissipated by radiative heat transfer dynamics using a simple cylindrical cell?
- How do the heat transfer dynamics evolve at different discharge powers?
- How can the amount of radiative heat be increased (E-value)?
- What practical solutions can be applied to these questions?
- How significant will this application be for a given example?

The structure of this article is as follows: in Section 2, the Materials and Methods are explained in detail, Section 3 discusses the results and discussion, and Section 4 contains the relevant conclusions drawn from the results presented in the article.

2. Materials and Methods

The degree of radiation heat transfer can be determined using various measurement methods and strategies. The present study focuses on determining the exact heat generation and surface temperatures of battery cells. The contributions of different heat transfer mechanisms are identified by interpreting measurement results. When applying the method, it is essential to consider variables and dynamically changing parameters that influence cell heating [14]. Furthermore, a precise understanding of the thermophysical properties of the cell materials is required. Detailed mapping of the heat transfer processes is supported by numerical simulation models, which contribute to interpreting the measurement results [25]. To ensure the reliability of the simulations, input parameters from physical experiments and measurements are used to validate the cell model.

2.1. Method Development Computational Fluid Dynamics (CFD)

In the cases examined during the research, battery cells generate heat during discharge, which they transfer to their environment through various mechanisms. The heat transfer processes were modeled using numerical simulation tools. The Computational Fluid Dynamics method enables the accurate modeling of heat transfer between solid bodies and fluid volumes, as well as between surfaces and electromagnetic waves, i.e., radiation processes, which are crucial to the research [26–28]. Various commercial and open-source simulation software platforms are available for modeling tasks. In modeling cylindrical battery cells, the open-source software OpenFOAM v2312 has proven to be an effective tool; however, for treating radiative heat transfer processes, the Ansys Fluent 2025R1 solver

provided a more robust and reliable solution. Therefore, Ansys Fluent was ultimately selected for the simulations to achieve the research objectives.

2.1.1. Heat Transfer Modeling

When modeling heat dissipation during a battery cell's discharge process, several key considerations must be taken into account. While the numerical methods and implementation of physical models may differ across various software platforms, the resulting simulation outcomes are generally consistent and comparable [29,30]. Consequently, the following sections focus exclusively on the physical modeling approaches employed by the selected simulation tool. The initial phase of the battery simulation setup involved a comprehensive analysis of the energy conservation equation and the associated models utilized for its resolution. The specific form of the energy transport equation adopted by the selected solver is provided in Equation (2).

$$\frac{\partial(\rho E)}{\partial t} + \nabla[V(\rho E + p)] = \nabla \left[K_{eff} \nabla T - \sum_j h_j J_j + \tau_{eff} V \right] + S_h \quad (2)$$

where ρ is the density (kg/m^3), V is the overall velocity vector (m/s), E is the total energy, activation energy (J), p is the pressure (Pa), K_{eff} is the effective conductivity ($k + k_t$, where k_t is the turbulent thermal conductivity, defined according to the turbulence model being used), and J_j is the diffusion flux of species j , T is the temperature (K), h_j is the Sensible enthalpy (energy/mass), τ_{eff} is the Stress tensor (Pa), S_h includes the heat of chemical reaction and any other volumetric heat sources that have been defined [31].

To develop a realistic thermal model of a battery, it is crucial to accurately quantify the thermal energy generated within the cell, the conduction of heat through solid materials, the heat transfer across contact surfaces between components, the convective heat exchange between solid bodies and surrounding gases, and the radiative heat transfer mediated by electromagnetic waves. Accordingly, the following heat transfer models are required: conduction, convection, radiation, and electrochemical heat [11,31,32].

In modeling thermal conductivity within the material, several assumptions must be introduced, which, although they inevitably lead to deviations from the actual physical behavior, are necessary to ensure the practical applicability of the model. These assumptions primarily pertain to the material properties. Initially, the heat generated by the battery's electrochemical reactions is defined as a volumetric heat source. Subsequently, accurate computation of the energy flow requires knowledge of the material's density, specific heat capacity, and thermal conductivity. The software evaluates the energy equation within the solid regions based on Equation (3).

$$\frac{\partial(\rho h)}{\partial t} + \nabla(v\rho h) = \nabla(k\nabla T) + S_h \quad (3)$$

where ρ is the density, h is the sensible enthalpy (energy/mass), k is the conductivity ($\text{W}/(\text{mK})$), T is the temperature (K), and at the end, S_h is the volumetric heat source ($\text{W}/(\text{m}^3\text{K})$) [24]. Therefore, several assumptions are made here to simplify further the calculation of the battery temperature field [31].

Natural convection refers to the motion of a fluid induced by density differences (buoyancy) resulting from temperature gradients [31]. This physical phenomenon must be considered in the thermal modeling process. Convective flows are expected to develop within the air gaps of varying volumes between cells as their temperatures increase. Therefore, it is necessary to construct a fluid dynamics framework within the simulation model with sufficient precision to capture convective phenomena accurately. Among the

fundamental parameters governing fluid dynamics, the specification of pressure, density, viscosity, temperature, and gravitational acceleration is essential. Upon including gravitational effects, the momentum equation takes the following form (Equation (4)) [31]. The simulation defines gravitational acceleration as 9.81 m/s^2 along the Z-axis. The momentum equation in the Z-direction is provided in Equation (4).

$$\frac{\partial(\rho W)}{\partial t} + \nabla(\rho UW) = \mu \nabla^2 W - \frac{\partial P'}{\partial z} + (\rho - \rho_0) g \quad (4)$$

where ρ is the density, W is the direction Z in the Descartes coordinate system, U represents the free-stream velocity (m/s), μ is the dynamic viscosity (Pa.s), P is the pressure (Pa), g is the gravitational acceleration (m/s^2), ρ and ρ_0 are the density and operation density (kg/m^3) [31].

An important consideration regarding the definition of pressure is that the air domain is modeled using an incompressible-ideal gas approach. Under this assumption, the air density is treated as a function of the reference pressure and temperature, as described in [31]. The incompressible-ideal gas model is particularly suitable when pressure variations are negligible while temperature variations are significant. In this formulation, the fluid density is considered a function of temperature alone. When these conditions are met, the incompressible-ideal gas model exhibits better convergence behavior than the full ideal gas law, with minimal loss of accuracy [31]. The relationship is expressed in Equation (5).

$$\rho_0 = \left(\frac{P_{op} M}{RT} \right)_{\text{average}} \quad (5)$$

where a P_{op} is the ambient pressure (operation conditions), M is the molecular weight, and R is the universal gas constant.

2.1.2. Radiation Modeling

Radiation constitutes the third primary heat transfer mechanism, following convection and conduction. Radiative heat transfer between two objects situated within non-absorbing and non-emitting media is governed by the Stefan–Boltzmann law, as expressed in Equation (6) [4,26].

$$Q_{rad} = F_{1-2} \cdot \varepsilon_1 \cdot A_1 \cdot \sigma \cdot (T_2^4 - T_1^4) \quad (6)$$

where Q_{rad} is the radiation heat transfer rate ($\text{W/m}^2\text{K}$), F_{1-2} represents the view factor between two objects, ε_1 is the dimensionless emissivity or absorptivity, A_1 represents the surface area of object one, σ is the Stefan–Boltzmann constant ($5.69 \times 10^{-8} \text{ W/(m}^2\text{K}^4)$), and T_1 and T_2 are the surface temperature of objects.

Radiation can be treated either as a volumetric or a surface phenomenon. This mode of heat transfer plays a critical role in studying heating, cooling, drying, combustion, solar radiation, and various other industrial processes. In the present case, the medium surrounding the battery cell is ambient air of general composition at room temperature, which can be considered transparent to radiation as it does not absorb radiative energy. All surfaces in the model are non-transparent, and the geometry is relatively simple; therefore, radiation is treated as a surface phenomenon. Under these boundary conditions, the “surface-to-surface” (S2S) radiation model offered by the selected simulation software is deemed the most appropriate choice [27,28,31].

Verdério et al. [33] investigated radiative heat transfer between a cylindrical body and enclosing walls, comparing the Finite Volume Discrete Ordinates Method (FVDOM) with the surface-to-surface (S2S) model. Their study explicitly resolved the air volume in the FVDOM approach but neglected under the S2S (view factors) model. Validation of the simulation

results for both methods confirmed that omitting the air domain introduces negligible error while substantially reducing computational demands. However, the authors emphasized that this simplification is primarily effective for simple geometry cases. The surface-to-surface (S2S) radiation model is well-suited for simulating radiative heat exchange between boundaries without accounting for the participating media in between. This implies that no absorption, scattering, or emission occurs within the medium, and radiative energy transfer is limited to surface interactions. The energy exchanged between two surfaces depends on factors such as surface area, separation distance, and relative orientation [31]. These geometric dependencies are captured by the view factor, which quantifies the fraction of radiation leaving one surface that directly reaches another. The S2S model is based on this concept, with view factors computed by the software using geometric relationships and line-of-sight visibility. The net radiative energy flux leaving a given surface consists of both emitted and reflected components. The reflected portion depends on the incoming radiative flux from surrounding surfaces, which can, in turn, be expressed as a function of the outgoing fluxes from all other surfaces [31]. The total energy flux leaving surface K is defined as follows (see Equation (7)):

$$Q_{out,k} = \varepsilon_k \cdot \sigma T_k^4 + (1 - \varepsilon_k) \cdot \sum_{j=1}^N F_{kj} q_{out,j} \quad (7)$$

where $q_{out,k}$ is the energy flux leaving the surface, ε_k is the emissivity, σ is the Stefan-Boltzmann constant, $q_{in,k}$ is the energy flux incident on the surface from the surroundings, and F_{jk} is the view factor between surface k and surface j . The view factor between the two finite surfaces (surface k and surface j) is given by the following (see Equation (8)):

$$F_{kj} = \frac{1}{A} \int_{A_k} \int_{A_j} \frac{\cos\theta_k \cos\theta_j}{\pi r^2} \delta_{kj} dA_k dA_j \quad (8)$$

where δ_{kj} is determined by the visibility of dA_j and dA_k , $\delta_{kj} = 1$ if dA_j is visible to dA_k and 0 otherwise.

2.1.3. Heat Generation Modeling

This study aims to apply a cost-effective modeling approach that does not explicitly resolve electrochemical processes yet can accurately estimate the heat generation dynamics of Li-ion batteries and their variation as a function of the state of charge (SOC). For this purpose, the input parameter for the numerical model is the value of Q_{gen} [W/m^3], determining the heat generation for the solid domain representing the battery, corresponding to the given SOC value. This methodology enables a computationally efficient thermal modeling solution with satisfactory accuracy [9–11,13,14,34]. The Bernardi equation was employed to estimate the heat generation, which describes the heat produced within the cell, as shown in Equation (9) [10].

$$Q_{gen} = I(V_{oc} - V) - I \left(T \frac{dV_{oc}}{dT} \right) \quad (9)$$

where the Q_{gen} is the generated heat by the battery cell (W); I is the current (A), V and V_{oc} are the voltage under load and the open circuit voltage, respectively (V); the T is the battery cell surface temperature (K); and the $\frac{dV_{oc}}{dT}$ is the entropic term.

The thermal model distinguishes two primary heat components: irreversible (ohmic) heat and reversible (entropic) heat. Accurate estimation of ohmic heat generation requires knowledge of the open-circuit voltage (OCV), as the difference between the cell voltage and the OCV appears directly in the first term of the Bernardi equation. However, experimental

determination of the OCV–SOC characteristic for a given cell type is a time- and resource-intensive process, typically involving low-current charge-discharge cycles and extended rest periods [13,35–41]. To calculate the ohmic heat, the table-based OCV–SOC curve presented by Sundaresan et al. [42] was utilized, which is based on the same cell type used in the present study. This approach implements the so-called “combined +3” model, which accurately captures the OCV behavior of real cells across the full SOC range (see Equation (10)).

$$V^\circ(s) = k_0 + \frac{k_1}{s} + \frac{k_2}{s^2} + \frac{k_3}{s^3} + \frac{k_4}{s^4} + k_5 s + k_6 \ln(s) + k_7 \ln(1-s) \quad (10)$$

where s is the normalized SOC value and $k_0 \dots k_7$ are the parameters fitted to the curve. The entropic coefficient required for reversible heat generation, dV_{oc}/dT , was adopted from Han et al. [43], who determined its SOC dependence using inverse heat transfer analysis (IHTA). The investigated cell type (Samsung INR21700-50G, NCA/graphite chemistry) is compatible with the cell used in this study. The IHTA method enables rapid and accurate parameter estimation while significantly reducing experimental time compared to conventional potentiometric techniques. The energy balance equation derived the entropic term (see Equation (11)).

$$\frac{dU_{oc}}{dT}(t) = \frac{mc_p \frac{dT}{dt} - I(U_{oc} - V_{cell}) + h \cdot A(T_{cell} - T_{amb})}{IT_{cell}} \quad (11)$$

where m is the mass of the cell, c_p is the specific heat capacity, T_{cell} is the cell temperature, T_{amb} is the ambient temperature, I is the current, U_{oc} is the open-circuit voltage (OCV), V_{cell} is the cell output voltage, and $h \cdot A$ is the heat transfer coefficient multiplied by the cell surface area. According to the literature, the SOC dependence of the entropic coefficient exhibits a consistent trend across varying discharge rates. A key advantage of the present model is that temperature–time curves obtained from experimental measurements are not used directly to derive heat generation terms; instead, they serve as calibration references to ensure the thermal realism of the simulation. In contrast, the heat generation dynamics and entropic coefficient are adopted from validated literature models [43] based on high-resolution and controlled experimental data. This hybrid approach enables the implementation of a simplified yet validated thermal model tailored to the study’s objectives.

2.2. Physical Testing

Laboratory measurements are essential for calibrating and validating the thermal model, particularly for accurately defining the temperature range and heat generation levels. Recorded data include voltage and current at the cell terminals, surface temperatures of the cell, and ambient temperature inside the measurement chamber.

All charging, discharging, and relaxation phases during the physical measurements were conducted under controlled conditions. The cell charging process was carried out using the constant current–constant voltage (CC–CV) method. The constant current phase was performed at a rate of 0.5C until the cutoff voltage of 4.2 V was reached, followed by a constant voltage phase, during which the voltage was held at 4.2 V until the current dropped below [e.g., 0.05C or 250 mA]. This point was defined as the fully charged state.

During the discharging experiments, the cells were discharged at a given constant C-rate down to the cutoff voltage of 2.5 V, as specified for this particular cell type.

Experiments were conducted in a custom-designed, low-volume test chamber that ensures stable environmental conditions and minimizes external thermal disturbances. Temperature measurements were performed using multiple sensors placed at various positions on the cell and in the surrounding air. The cell environment was continuously

maintained under controlled conditions, with no interruptions. The test chamber remained sealed throughout the entire procedure, the test chamber shown in Figure 2

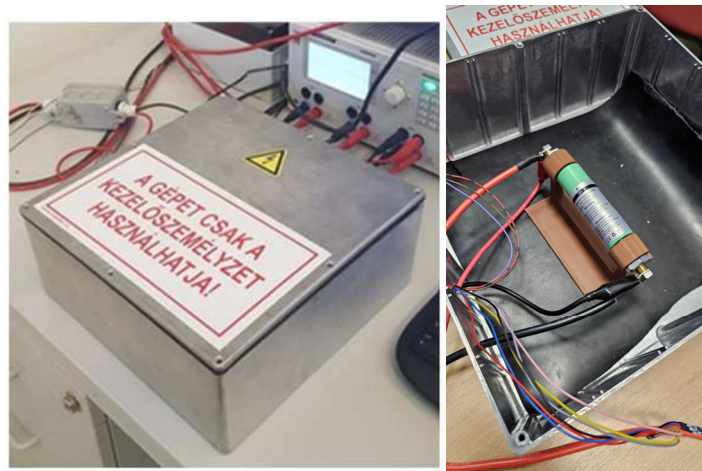


Figure 2. Showing the measurement chamber setting of the experimental measurement.

To maximize radiative heat transfer, the inner walls of the measurement chamber were given a high emissivity factor ($\epsilon \approx 0.9$), which was achieved by applying a polymer layer on the aluminum box's top and bottom walls.

Three battery cell configurations were analyzed in this study. In the baseline (BASE) case, the cell is free from any coating or covering, and the bare aluminum can serve as the only interface between the cell and its surroundings. This configuration exhibits the lowest surface emissivity ($\epsilon \approx 0.1$ [12,44]), resulting in minimal radiative heat transfer. In the second configuration, the cell is covered with a factory-applied colored plastic film, which increases the surface emissivity ($\epsilon \approx 0.65$ [8]) and thus enhances radiative heat dissipation. Due to the negligible thickness of the film, its influence on conductive and convective heat transfer is considered insignificant. The third case involves a tightly fitted, 3D-printed polymer casing that ensures good thermal contact with the cell surface, thereby facilitating effective conductive heat transfer. Due to its substantial wall thickness, the casing's thermal insulation and absorption properties must also be taken into account. This setup represents a potential structural element in a modular battery system. The polymer enclosure's surface emissivity can be increased significantly ($\epsilon \approx 0.95$ [44]), improving the radiative heat transfer performance through optimized design and printing parameters.

Based on the initial temperature distribution results of the CFD simulations, the highest surface temperatures, closest to the peak temperature of the electrochemically active zone, occur at the top of the cell, as shown in Figure 3. However, it is important to note that the temperature differences between the regions are relatively small. Nevertheless, if the goal is to minimize disturbance to the natural airflow around the cell, the top region also appears to be the most practical location for sensor placement (Figure 4, Section (B)—wall shear stress distribution). The test apparatus was designed to maximize the cylindrical surface area available for radiation and to accommodate precise sensor placement and stable casing integration. A minimal contact surface was used to reduce the potential for heat transfer to the test jig. Additionally, all other equipment in the test environment was coated with rubberized mats to minimize the risk of radiative heat being reflected to the battery. The custom measurement setup used for testing is shown in Figure 5.

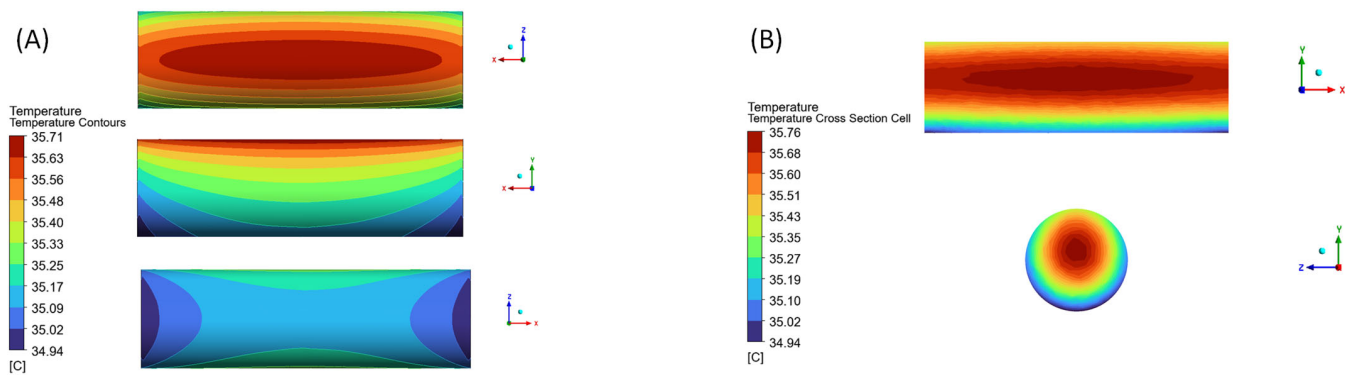


Figure 3. (A) Temperature distribution at $1\times C$ discharge of the cell surface (local temperature range). (B) Temperature distribution at $1\times C$ discharge of the cross-section of the cell (local temperature range).

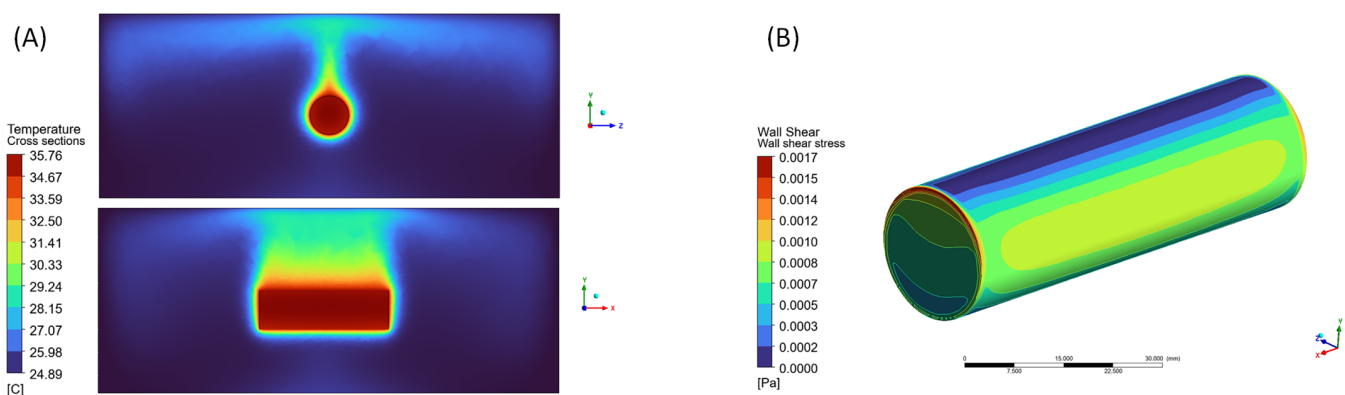


Figure 4. (A) Temperature distribution at $1\times C$ discharge in the chamber and cell domain and the effect of natural convection shown using cross-section views (global temperature range); (B) wall shear stress distribution on the cell surface at $1\times C$ discharge (local wall shear range).

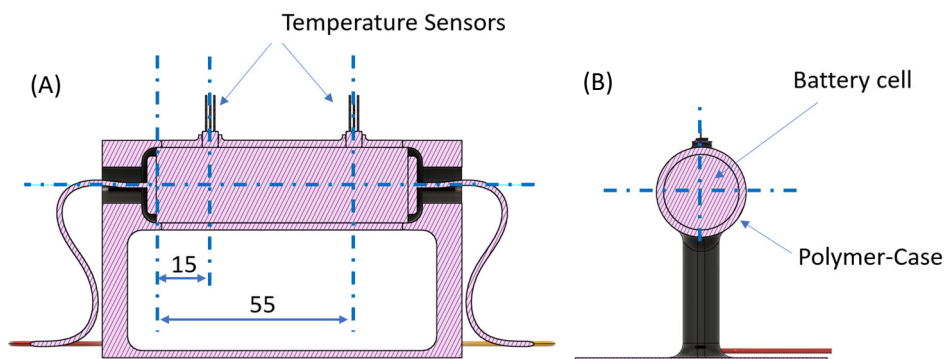


Figure 5. (A) Section view of a 21700 battery cell with cover in the test jig; (B) section view of a 21700 battery cell with cover in the test jig.

In each measurement, two LMT85 temperature sensors were placed on the surface of the cell, which offer a typical accuracy of $\pm 0.4\text{ }^{\circ}\text{C}$ in the $-20\text{ }^{\circ}\text{C}$ to $+100\text{ }^{\circ}\text{C}$ range. These sensors were directly attached to the surface of the cell as well as placed inside the sealed test chamber to monitor the ambient temperature. The sensor positions remained focused on the same area even during measurements with the polymer casing, as the casing was designed to be in direct contact with the top surface of the cell. Due to their small size and fast thermal response, the LMT85 sensors ensured accurate tracking of rapid thermal changes, and at the same time, the sensors are expected to have only a minor impact on the measurement results, primarily by locally reducing the active surface area of the polymer layer involved in heat transfer.

Although the thermal model calibration was based on discharge measurements, the charging phase was also performed under controlled conditions (CC–CV method) and is included for completeness. Table 1 presents the accuracy specifications of the physical measurement setup used in this study.

Table 1. Accuracy of the physical testing parameters.

| Parameter | Instrument/Sensor | Range/Resolution | Estimated Uncertainty | Type |
|----------------------|---|-------------------------|-------------------------------------|-------------|
| Current (I) | Elektro-Automatik EL3160-60A (load) (Viersen, Germany) | 0–60 A, 1 mA resolution | ±0.5% of reading ±20 mA | Absolute/±% |
| Voltage (U) | NI 9201 DAQ (12-bit, ±10 V range) (Austin, TX, USA) | ~4.88 mV resolution | ±25 mV typical | Absolute |
| Temperature (T_cell) | LMT85 analog sensor (Texas Instruments, USA) | −50 °C to +130 °C | ±0.4 °C (typical, −20 °C to 100 °C) | Absolute |
| Time (t) | NI system clock via LabVIEW control (Version 14.0.1f11) | — | <±0.1 s | Negligible |

The placement of the cells was carefully designed to optimize the radiative heat transfer path between the cylindrical cell surface and the chamber walls. The cell was centrally positioned within the chamber, maintaining an equal distance from all walls, thereby ensuring symmetric radiative heat exchange conditions (see Figure 6).

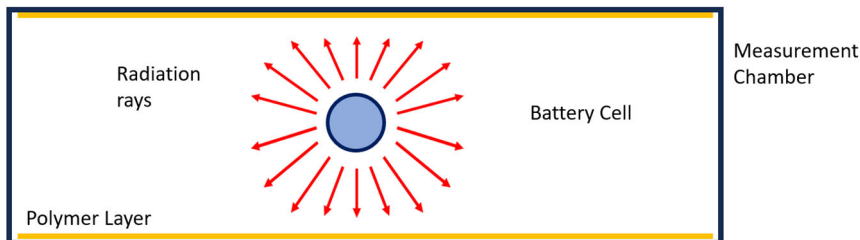


Figure 6. Radiative heat transfer from a centrally placed 21700 battery cell.

After initial formation measurement, new cells were subjected to constant current discharge tests at $1 \times C$, $2 \times C$, $3 \times C$, $4 \times C$, and $5 \times C$, with a separate measurement series conducted for each discharge rate (see Table 2). Adequate rest periods were provided between tests to allow thermal equilibrium to re-establish. Current, voltage, and temperature data were recorded using a high-resolution data acquisition system.

Table 2. Testing matrix.

| Case Number | BASE (Pure Cell Can) | Label (Cell Can with Colored Label) | BASE + Polymer Case |
|-------------|----------------------|-------------------------------------|---------------------|
| 1 | $1 \times C$ | $1 \times C$ | $1 \times C$ |
| 2 | $2 \times C$ | $2 \times C$ | $2 \times C$ |
| 3 | $3 \times C$ | $3 \times C$ | $3 \times C$ |
| 4 | $4 \times C$ | $4 \times C$ | $4 \times C$ |
| 5 | $5 \times C$ | $5 \times C$ | $5 \times C$ |

For safety reasons, physical discharge tests at $4\times C$ and $5\times C$ rates were terminated before reaching a full depth of discharge. In these cases, the surface temperature of the cells approached $+70\text{ }^{\circ}\text{C}$. Without active cooling, continued discharge would have posed a risk of cell degradation and potential safety hazards. However, the hybrid modeling approach described above allows the virtual completion of the entire discharge process by utilizing the acquired input parameters.

2.3. CFD Model Parameters

The simulation environment encompasses the entire volume of the measurement chamber and the battery cell positioned within it. External ambient conditions are defined via boundary settings, with a 10 W/m^2 heat flux applied on the outer chamber walls to represent heat exchange with the room-temperature environment. The active cell volume (jelly-roll) is modeled as a homogenized composite solid core, where the thermal properties of individual components are averaged into effective values. Material properties were assigned based on literature sources, with particular attention to anisotropic thermal conductivity, as heat conduction is significantly higher along the axial direction compared to the radial direction [32,45]. The detailed properties of the modeled regions can be seen in Table 3.

Table 3. Solid battery domain parameters.

| Regions | Material | Dimension (mm) | Density (kg/m^3) | Specific Heat (J/(kg K)) | Thermal Conductivity |
|-----------|-----------|-----------------------------|-----------------------------|-------------------------------------|--|
| Fluid | Air | $250 \times 250 \times 100$ | Incompressible ideal gas | 1003 | 0.025 |
| Cell Core | Composite | $D = 21\text{ h} = 70$ | 2500 | 900 | Radial direction = 1.106 Axial direction = 20 |
| Cell Can | Al | Thickness = 0.35 | 2790 | 903 | 238 |
| PVC Label | PVC | Thickness = 0.10 | 920 | 1000 | 0.334 |
| PLA Case | PLA | Thickness = 2.00 | 1430 | 1800 | 0.13 |

In addition to the active cell volume, the cell can and external foil layer were modeled using designated shell regions, shown in Figure 7. This approach enables the construction of a robust finite element mesh with a low element count while maintaining the required thermal accuracy by applying appropriate $1\times D$ and $2\times D$ thermal conductivity properties.

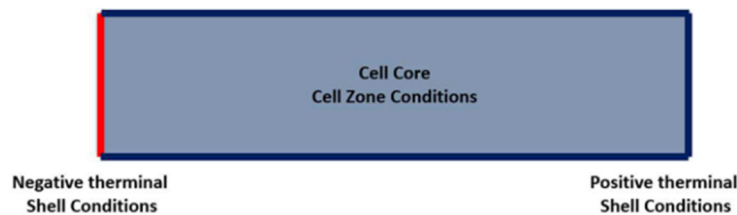


Figure 7. The simplified battery cell model using cell core and shell regions.

Radiative heat transfer conditions were established by assigning emissivity values to the boundary surfaces. Depending on the simulation scenario, specific emissivity values were applied to both the chamber walls and the cell surface.

2.3.1. Mesh Settings

During the optimization of the CFD simulation, various boundary condition strategies were tested, including the application of surface thermal resistances, the definition of shell regions, and a detailed mesh independence analysis. The meshing tests revealed that below

a surface element size of 3 mm, the variation in the cell's surface temperature became negligible. Based on this, the optimal element size was determined to be 1 mm, as shown in Figure 8. To accurately model the airflow around the cell, a five-layer boundary layer was implemented along the walls of the fluid domain. With this configuration, sufficient numerical accuracy was ensured even at the highest flow velocities (using the $k-\omega$ SST turbulence model, wall $y^+ < 1$).

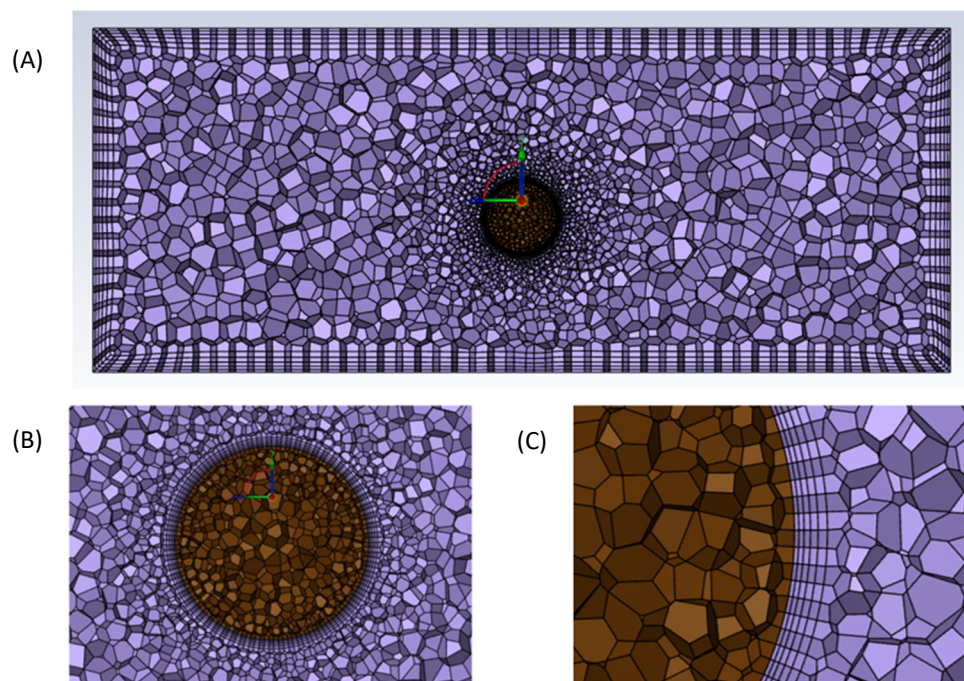


Figure 8. (A) Cross-section view of the chamber environment with the position of the cell; (B) close look of the cross-section of the battery cell; (C) close look of the boundary layer and mesh element on the surface of the cell. The purple areas of the mesh represent the chamber air, while the brown cylindrical region corresponds to the battery cell.

2.3.2. Shell Layer vs. Case Geometry in the Mesh

The simulation software provides the option to omit the physical meshing of the LABEL or polymer-casing layers under investigation. This reduces the model complexity and decreases the required computational time (CPU time). The software allows the definition of thermal resistance on wall boundaries, where the layer thickness and material properties are specified. In this case, the software treats the layer as a one-dimensional model in calculating the heat flux during the energy equation solution. However, this approach is not suitable for detailed spatial modeling of the temperature distribution, as the heat transfer is only calculated in the direction normal to the wall surface.

The use of shell regions enables more accurate thermal modeling. In this approach, the software assigns virtual cells to the regions, allowing heat transfer to be modeled in all directions (see Figures 9 and 10). Since shell regions support more detailed thermal analysis and the specification of layers with varying thicknesses and material properties, this method is better suited to the objectives of the present study.

The application of shell regions allows different parameters to be defined on the wall and wall-shadow surface pairs, provided the appropriate physical models are selected. This is particularly advantageous in radiation modeling, as it enables the specification of distinct surface properties when using the DO (Discrete Ordinates) or Surface Photon Monte Carlo models. In contrast, the S2S (surface-to-surface) model represents a much simpler approach. It does not support the definition of detailed optical boundary conditions, but it

is significantly more cost-efficient in terms of computational requirements. Accordingly, comparative simulation tests were carried out using the S2S model in order to quantify the magnitude of the systematic error introduced by its application.

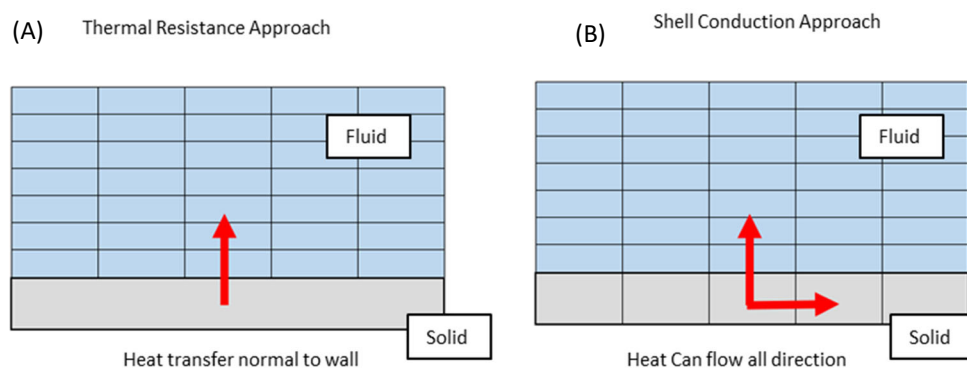


Figure 9. (A) Heat transfer across thermal resistance approach; (B) heat transfer across shell conduction approach. The grey regions represent virtual mesh elements within the solid shell region, while the blue areas correspond to the mesh of the fluid domain. Red arrows indicate the direction of heat transfer.

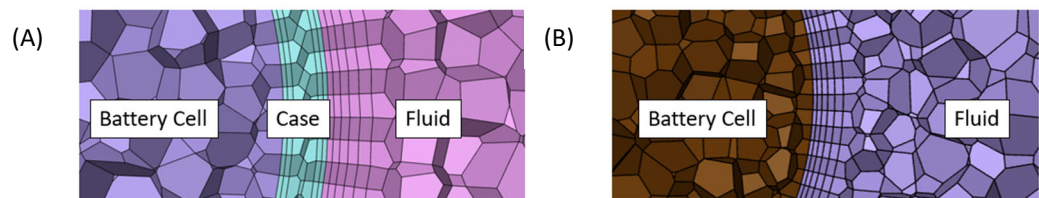


Figure 10. (A) Cross-section of the initial mesh when the polymer case was in the CAD; (B) cross-section of the initial mesh when shell conduction was used to model the polymer case; the shell region was only generated during the initialization phase.

2.3.3. Radiation Model Evaluation

The simulation software allows the use of various models for radiative heat transfer, including the S2S, DO, and Surface Photon Monte Carlo methods. During the simulation optimization, all three models were tested. The primary advantage of the DO and Monte Carlo models is their ability to accurately model radiation transport both between surfaces and through participating media. As a result, they offer greater accuracy compared to the S2S model, which only accounts for surface-to-surface heat transfer and neglects the influence of the medium.

However, since both the applied PVC film and the polymer casing are non-transparent and have a negligible wall thickness, the error introduced by using the S2S model can be considered insignificant for the investigated results. This was validated through multiple simulation cycles using identical mesh resolutions and material properties, as shown in Tables 4–6. In the initial simulations, particularly under the highest discharge power, temperature deviations of 1–2 °C were observed. Nevertheless, as the resolution of the radiation models was increased, the results began to converge toward a common temperature value.

At increased resolution, the maximum temperature predicted by the S2S model was 0.34 °C lower than that of the DO model and 0.64 °C higher than the value obtained with the Monte Carlo model. The temperature rise curves and the surface temperature distribution of the cell followed the same trend across all three models. The most significant difference, however, was observed in the required computation time: the S2S model provided a substantial advantage in this regard, with a reduction of 78% and 73% in computation time compared to the DO and Monte Carlo models, respectively.

(The simulations were performed on a 12th-generation Intel Core notebook CPU using four processor cores.)

Table 4. Simulation domain parameters.

| Regions | Material | Dimension (mm) | Density (kg/m ³) | Specific Heat (J/(kg K)) | Thermal Conductivity |
|-----------|-----------|------------------|------------------------------|--------------------------|--|
| Fluid | Air | 250 × 250 × 100 | Incompressible ideal gas | 1003 | 0.025 |
| Cell Core | Composite | D = 21 h = 70 | 2500 | 900 | Radial direction = 1.106 Axial direction = 20 |
| Cell Can | Al | Thickness = 0.35 | 2790 | 903 | 238 |
| PVC Label | PVC | Thickness = 0.10 | 920 | 1000 | 0.334 |
| PLA Case | PLA | Thickness = 2.00 | 1430 | 1800 | 0.13 |

Table 5. Optical parameters of the cell's external layers.

| | Material | Thickness (mm) | Refractivity Index | Surface Emissivity | Diffuse Fraction | Absorption Coefficient | Scattering Coefficient (m ⁻¹) |
|----------|----------|----------------|--------------------|--------------------|------------------|------------------------|---|
| Cell Can | Al | 0.3 | 1.5 | 0.1 | 0.1 | 1×10^7 | 0 |
| Label | PVC | 0.1 | 1.5 | 0.65 | 1 | 10,000 | 1000 |
| Case | PLA | 2 | 1.5 | 0.95 | 1 | 10,000 | 1000 |

Table 6. Optical parameters of the chamber walls.

| Chamber Wall Properties | Material | Thickness (mm) | Emissivity | Diffuse Fraction |
|-------------------------|----------|----------------|------------|------------------|
| Side | Al | 2 | 0.2 | 0.1 |
| Bottom | Al | 2 | 0.95 | 1 |
| Top | Al | 2 | 0.85 | 1 |

2.3.4. Material Properties Used for the Simulations

Tables 4–6 summarize the material properties used in the CFD simulations. These properties were defined based on values available in the literature and should, therefore, be considered as estimated parameters. The material properties of the actual materials used in the physical experiments were not directly measured [8,12,26,31,45,46].

3. Results and Discussion

3.1. Summary of the Measurements

In this series of measurements, the change in cell temperature during discharge of 21700 Li-ion battery cells at various constant discharge rates ($1\times C\dots 5\times C$) was investigated. The results depicted in the graph of Figure 11 illustrate that the change in cell surface temperature (ΔT) as a function of time shows a significant increase in the amount of heat generated by the cells with increasing discharge rate. The most significant temperature increase was observed for the $5\times C$ discharge rate, where ΔT reached $\sim 45\text{ }^\circ\text{C}$ in less than 500 s. In contrast, for the $1\times C$ rate, a temperature increase of $\sim 11\text{ }^\circ\text{C}$ was observed over more than 3000 s.

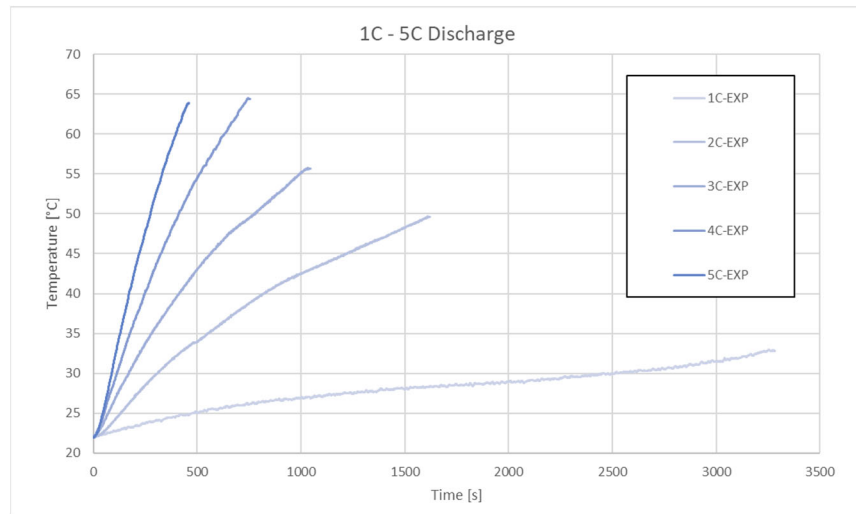


Figure 11. The 21700 battery discharge temperature.

The presented behavior reflects the combined effect of ohmic and entropic heat generation, i.e., the intensity of heat generation from internal resistance and electrochemical processes increases at higher discharge rates. Experimental data indicate that the discharge rate has a significant impact on the thermodynamic behavior, a key factor in designing thermal management systems. Note that the experiment was stopped for $4 \times C$ and $5 \times C$ discharges when the cell surface temperature reached $+70\text{ }^{\circ}\text{C}$. To ensure safe operation, follow the cell data sheet [5]. Thus, the experiment demonstrated that without a thermal management system, it is impossible to exploit the cells' maximum performance.

Heat Generation Model

The hybrid model results in a dynamically varying heat generation curve as a function of SOC during $1 \times C$ discharge (see Figure 12).

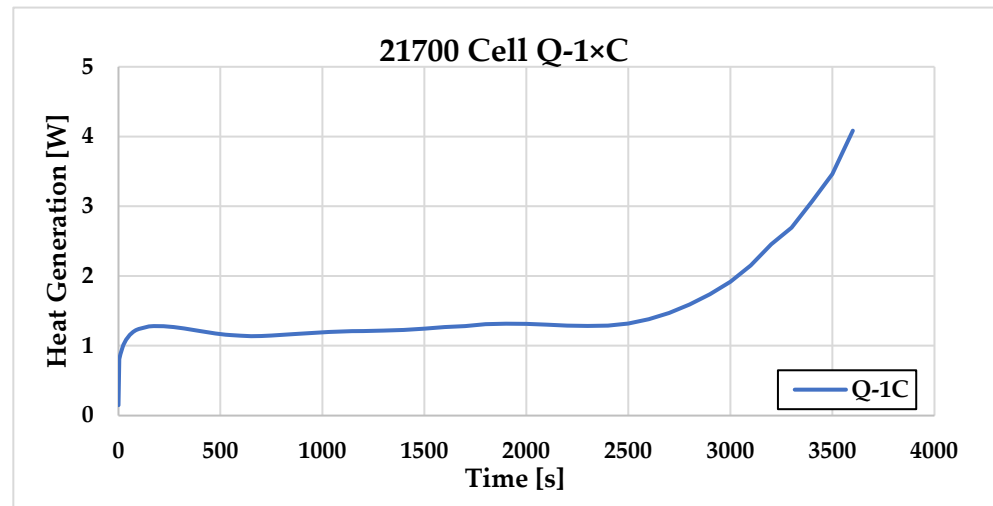


Figure 12. The 21700 cell heat generation chart at $1 \times C$ discharge.

The dynamics of the curve are in agreement with those of cylindrical cell heat generation curves published in the literature [9–11,13,14,34,47,48]. The initial rise is followed by a gradual fall, and then the heat production rate starts to rise again in the second half of the discharge, with a sudden spike at the end of the dip. This dynamic is also related to the dynamic change in the internal resistance of the cylindrical cells [47].

3.2. Simulation Cases and Correlation

Using the heat generation model and the cell geometry representation method described in the Section 2, the cases listed in the Section 2.2, Table 2, were simulated. Similar to physical testing, temperature measurements were always performed on the cell surface. The simulation results closely approximate the empirically observed, dynamically changing temperature curves, as summarized in Figure 13. This dynamic behavior is most evident during the $1 \times C$ discharge. At lower discharge rates, the phenomenon becomes even more pronounced. The temperature variations, influenced by changing internal resistance and entropic heat generation, cause greater fluctuations in terms of average heat generation values. At higher discharge rates, such as $4 \times C$ and $5 \times C$, the curve's trend approaches a linear increase. The most significant deviation between experimental and simulated values is observed during the $3 \times C$ and $4 \times C$ discharges. However, the dynamic behavior and overall trend remain consistent. Additional physical measurements and more input data could further enhance the model's accuracy.

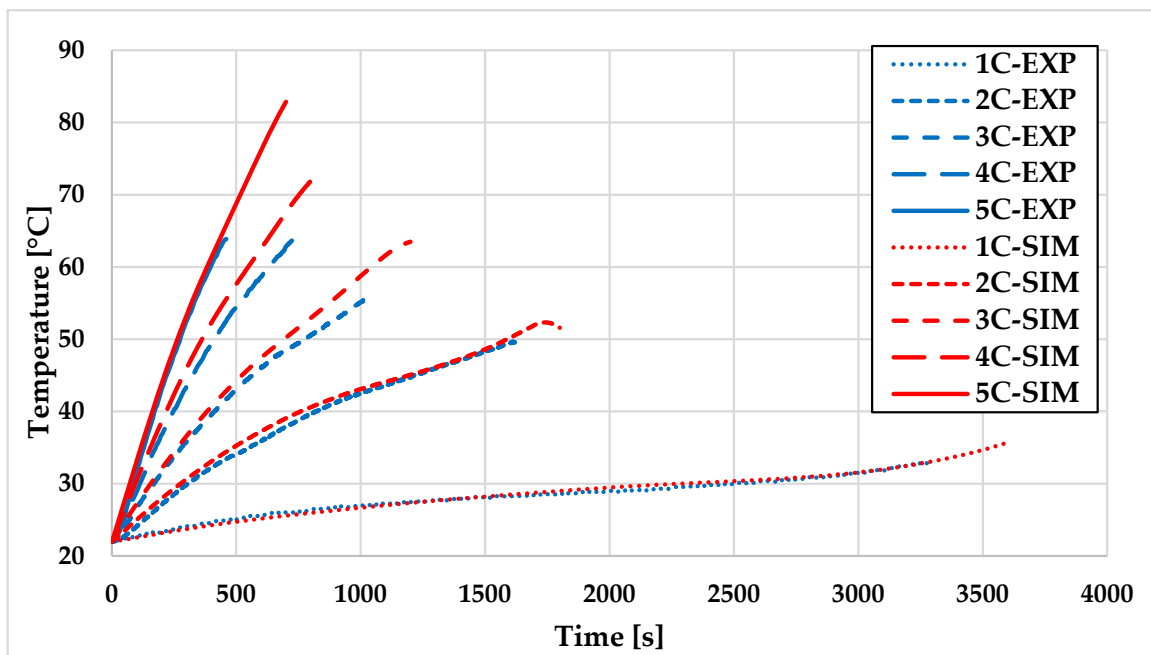


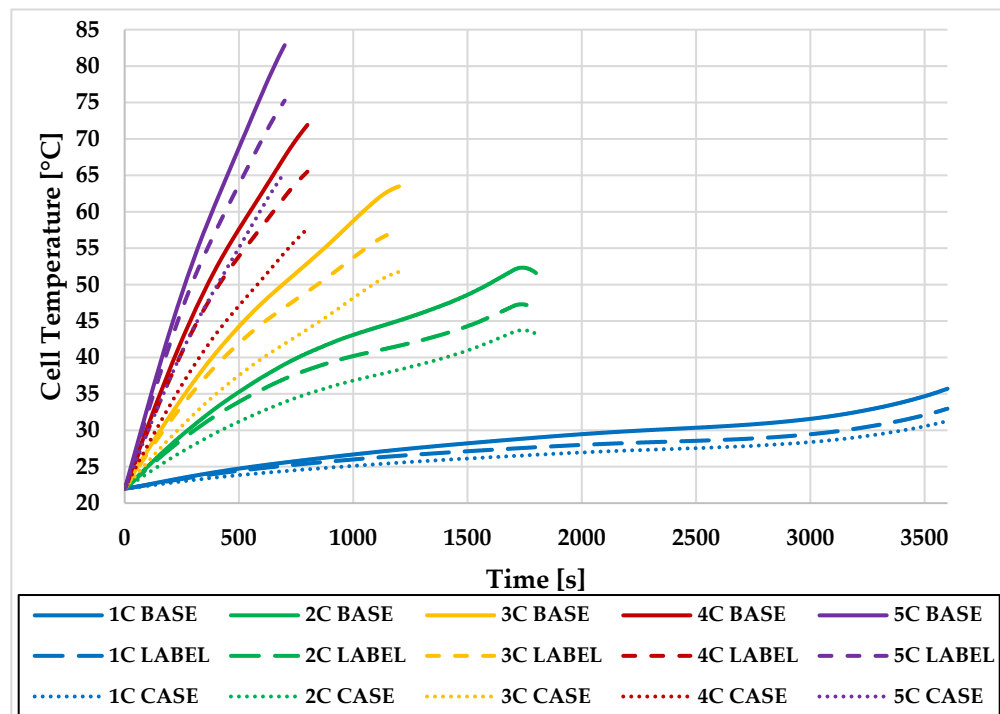
Figure 13. The $1 \times C$.. $5 \times C$ discharge temperature results of experimental and simulation results.

3.3. Temperature Evaluation Under Different Emissivity Conditions

The simulation results, at the same discharge power but with an increased surface emission factor, follow the trend predicted by the literature, more dominantly at high discharge and temperature conditions. Table 7 shows the highest temperature values in the simulated cases along all discharge and cell configurations. The label alone reduced the cell temperature during each discharge test. The temperature reduction rate increased steadily as discharge rates and temperatures increased. The polymer case configuration also led to a gradual improvement in cell temperature across all discharge conditions, further enhancing the results achieved in the label case. However, when examining the temperature profile trends, it becomes evident that in the base and label configurations, the curves closely follow one another, particularly during the initial stages of discharge, i.e., within the lower temperature range. In contrast, the polymer case shows a significant improvement from the very beginning of the discharge process (Figure 14). To better understand these trends, a detailed analysis of the heat transfer mechanisms was conducted.

Table 7. Heat transfer distribution at the end of each discharge test.

| Discharge | BASE | LABEL | CASE |
|-----------|---------------|---------------|---------------|
| | End Temp (°C) | End Temp (°C) | End Temp (°C) |
| 1C | 35.71 | 32.97 | 31.28 |
| 2C | 51.58 | 46.49 | 43.24 |
| 3C | 63.49 | 57.32 | 51.73 |
| 4C | 71.93 | 65.51 | 57.66 |
| 5C | 82.86 | 75.26 | 65.40 |

**Figure 14.** The $1 \times C \dots 5 \times C$ discharge temperature results of base, label, and polymer case cases.

3.4. Heat Transfer Mechanisms

Based on the temperature results of the simulation models developed for the base cases and with knowledge of the battery cell parameters, Equation (7) provides a means of analyzing the heat transferred to the environment. The relative contributions of convective and radiative heat transfer at discharge rates from $1 \times C$ to $5 \times C$, as well as their comparative results, are shown in Figures 15–17.

Regarding the BASE cases, as the discharge power increases, the overall heat dissipation also increases. Both convective and radiative heat transfer exhibit rising trends (Figure 15). However, while the growth in convective heat transfer demonstrates dynamic behavior that closely follows the cell's heat generation patterns—particularly at lower discharge rates (Figure 15)—radiative heat transfer shows a continuous but significantly more modest increase across all discharge levels (Figure 15). This difference is attributed mainly to the low emissivity value ($\varepsilon = 0.1$) specified among the input parameters, which aligns with the dominance of convective mechanisms, as shown in Figure 15. During both physical measurements and simulation scenarios, the initial chamber environment was maintained near room temperature, fluctuating between $+22^{\circ}\text{C}$ and $+25^{\circ}\text{C}$. The temperature of the air volume inside the test chamber did not increase significantly, further supporting the prevalence of convective heat transfer under these low ambient conditions.

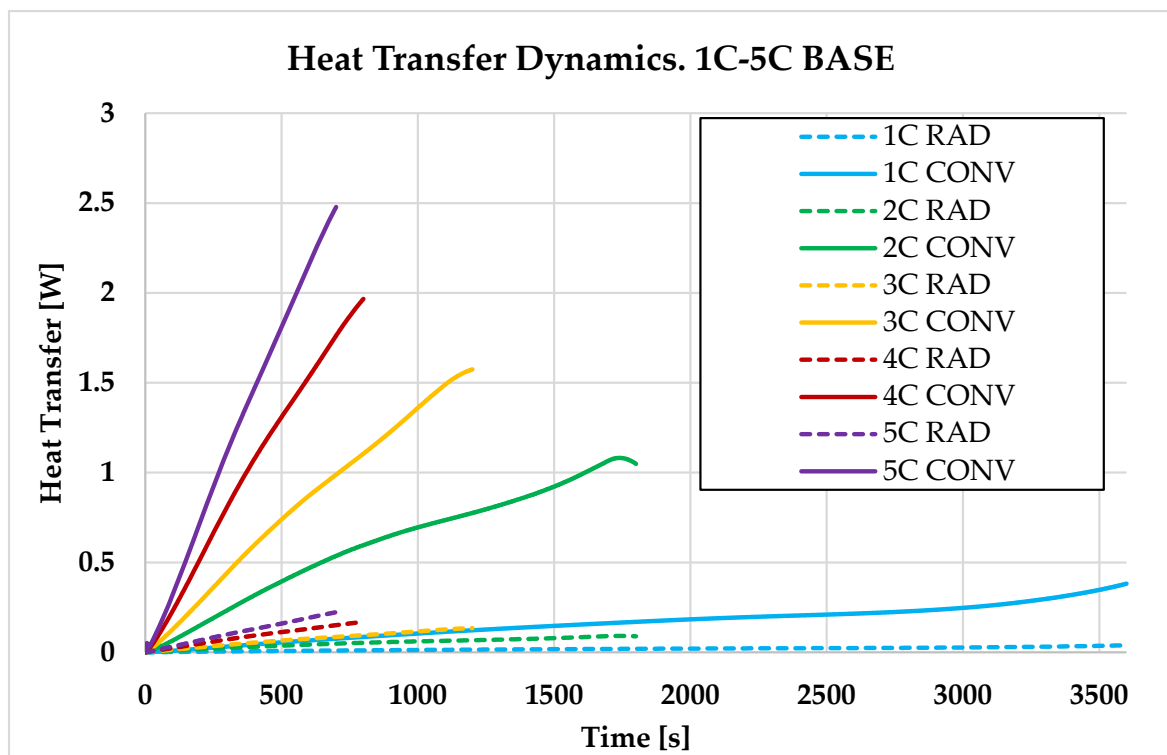


Figure 15. The figure illustrates the relative magnitudes of heat transfer dynamics during $1\times C \dots 5\times C$ discharges of the base case.

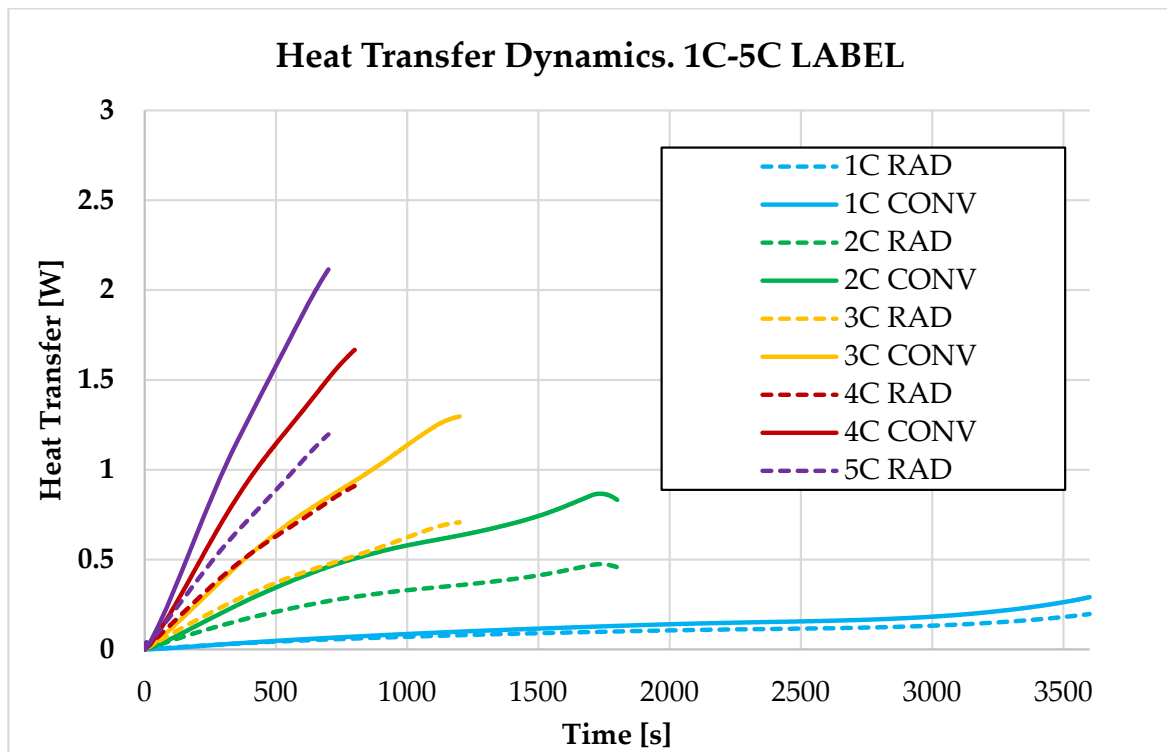


Figure 16. The figure illustrates the relative magnitudes of heat transfer dynamics during $1\times C \dots 5\times C$ discharges of label case.

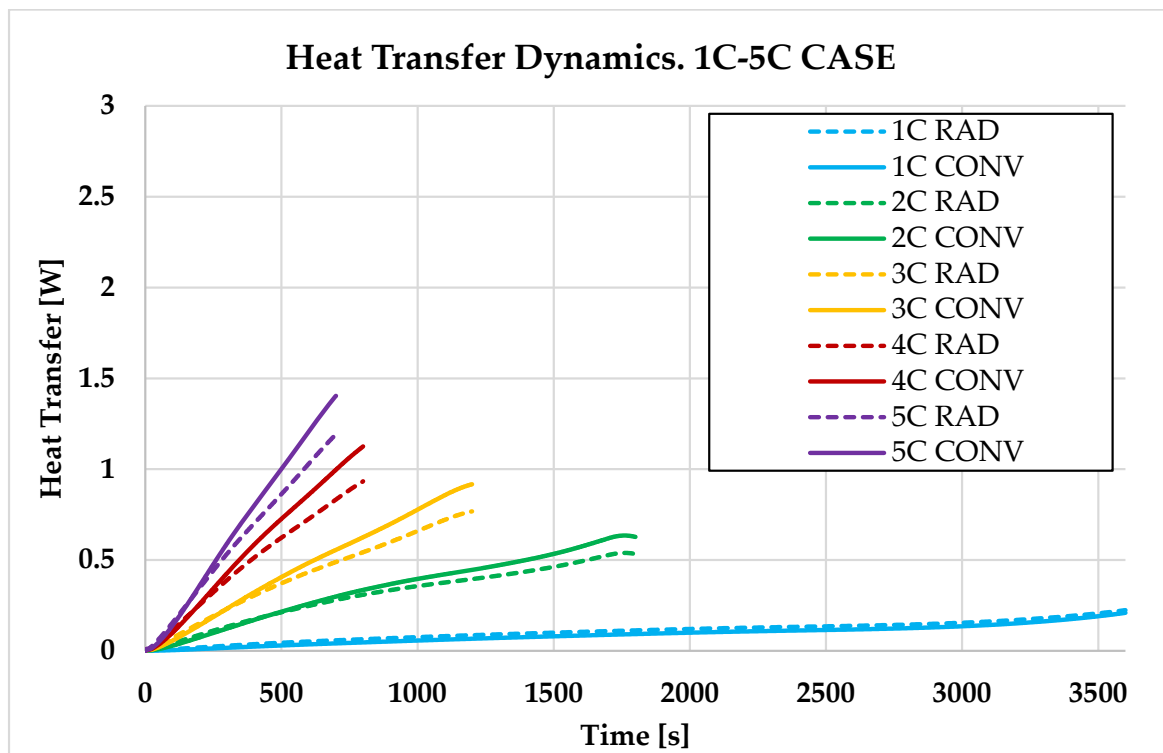


Figure 17. The figure illustrates the relative magnitudes of heat transfer dynamics during $1\times\text{C}\dots 5\times\text{C}$ discharges of the polymer case.

The significant temperature differences that developed between the cell surface and the surrounding measurement chamber continuously induced higher airflow velocities via natural convection, as illustrated in Table 8. This effect gradually increased the heat transfer coefficient measured at the cell surface. As a result, convective heat transfer, which was already the dominant mechanism even at low discharge rates, continued to intensify throughout the tests.

Consequently, the initially minor contribution of radiative heat transfer decreased further. However, this reduction was marginal, amounting to approximately only 1% of the total heat transfer. Therefore, in the base case, the ratio between convective and radiative heat transfer remained effectively constant throughout the test cycles.

To assess the impact of increased surface emissivity on overall heat transfer behavior, two enhanced-emissivity cases were investigated: the label ($\varepsilon = 0.65$) and polymer case ($\varepsilon = 0.95$) configurations. These aimed to intensify the role of radiative heat transfer within the total heat dissipation process, as visualized in Figures 16 and 17. Heat transfer dynamics were evaluated according to Equation (7).

Even in the label case, the elevated surface emissivity significantly increased the contribution of radiative heat transfer, raising it by orders of magnitude compared to the base case. This effect was further amplified in the polymer case configuration. Notably, under 1C discharge conditions, the maximum contribution of radiation to total heat transfer reached 40% in the label case and 52% in the polymer case.

As illustrated in Figures 15–17, radiative heat transfer was particularly effective during the initial phase of the discharge cycle. In fact, across all C-rates, radiation was able to briefly dominate the heat dissipation, surpassing convection, albeit by a small margin, especially in the polymer case scenario.

Table 8. Heat transfer distribution at the end of each discharge test.

| Discharge | BASE | | | | LABEL | | | | CASE | | | | | | |
|-----------|-------------------------|------------------------------------|-----------------------------------|---------------|--------------------------------------|-------------------------|------------------------------------|-----------------------------------|---------------|--------------------------------------|-------------------------|------------------------------------|-----------------------------------|---------------|--------------------------------------|
| | Total Heat Transfer (W) | Convection Heat Transfer Ratio (%) | Radiation Heat Transfer Ratio (%) | Airflow (m/s) | H _{tc} (W/m ² k) | Total Heat Transfer (W) | Convection Heat Transfer Ratio (%) | Radiation Heat Transfer Ratio (%) | Airflow (m/s) | H _{tc} (W/m ² k) | Total Heat Transfer (W) | Convection Heat Transfer Ratio (%) | Radiation Heat Transfer Ratio (%) | Airflow (m/s) | H _{tc} (W/m ² k) |
| 1C | 0.42 | 91% | 9% | 0.08 | 6.97 | 0.49 | 60% | 40% | 0.07 | 9.98 | 0.43 | 48% | 52% | 0.06 | 11.56 |
| 2C | 1.14 | 92% | 8% | 0.12 | 8.71 | 1.29 | 65% | 35% | 0.11 | 11.81 | 1.16 | 54% | 46% | 0.10 | 13.34 |
| 3C | 1.71 | 92% | 8% | 0.14 | 9.33 | 2.00 | 65% | 35% | 0.13 | 12.72 | 1.69 | 54% | 46% | 0.11 | 14.16 |
| 4C | 2.14 | 92% | 8% | 0.15 | 9.69 | 2.58 | 65% | 35% | 0.14 | 13.27 | 2.06 | 55% | 45% | 0.12 | 14.61 |
| 5C | 2.70 | 92% | 8% | 0.16 | 10.04 | 3.31 | 64% | 36% | 0.15 | 13.93 | 2.60 | 54% | 46% | 0.13 | 15.27 |

However, with increasing discharge rate, this balance shifts in favor of convective heat transfer. At 5C discharge, the relative share of radiation dropped to 36% for the label case and to 46% for the polymer case case (Table 8). It is important to note, however, that this does not imply an absolute reduction in radiative heat transfer. On the contrary, its absolute value continued to rise with the discharge rate, as demonstrated in Figures 15 and 16. The reason for the reduced proportional contribution is that convective heat transfer increases even more rapidly. This trend is supported by the total heat transfer values summarized in Table 8.

The increasing temperature of the cell enhances air circulation within the test chamber, which in turn boosts convective heat transfer at the surface. The highest convective velocities were observed in the base case, while the lowest was in the polymer case configuration, correlating directly with the maximum cell temperatures in each case.

When examining the maximum heat transfer rate across the external surface, the label configuration performed best. Conversely, the outer wall of the polymer case configuration exhibited the lowest overall heat transfer to the environment (Table 8). However, when considering only the cell surface heat transfer coefficient, the polymer case proved to be the most effective once again (Table 8).

To better understand this seemingly contradictory behavior, further analysis is presented in the following section.

3.5. Thermal Performance of Polymer Case Volume

It is important to highlight that in the polymer casing, the increase in convective heat transfer is consistently slower during the initial phase. Nevertheless, this configuration still performs better in the early stages compared to the label case. Explaining this phenomenon requires consideration of the polymer material's non-negligible volume and thermal properties. In the previous cases, heat generated by the cell core could dissipate relatively quickly to the environment via natural convection through the aluminum can. In contrast, the current configuration involves a longer heat transfer path due to the added wall thickness of the polymer casing. (As a reference, the polymer case wall thickness was 2 mm, while the label foil material thickness was only 0.1 mm.) This works favorably, as the cell can and the polymer case are tightly fitted, allowing for conjugate heat transfer between solid–solid interfaces. Initially, the casing effectively absorbs heat, helping to reduce the cell temperature. However, over the long term, the casing may act as a thermal insulator under basic discharge conditions, especially when radiative heat transfer remains minimal.

This case is illustrated in Figure 18 at a $5 \times C$ discharge rate. In both the base and label configurations, the temperature initially rises with a similar trend; however, as radiative heat transfer increases, the label case begins to diverge, resulting in a lower final temperature. In contrast, the polymer case configuration exhibits lower temperature values already from the initial phase. This is facilitated by the added wall thickness in the system, which initially aids in absorbing heat and is later supported by the increasingly significant radiative heat transfer, further reducing the cell temperature. As a result, under the highest load at $5 \times C$ discharge, the temperature reduction reaches up to 17°C .

In order to investigate the effect of the additional volume introduced by the polymer case, an extra simulation case, referred to as the extra label case, was conducted. In this setup, the surface emissivity in the simulation model was increased to $\epsilon = 0.95$, corresponding to the optical properties of the polymer case material. The results are also presented in Figure 18. The temperature profile of the extra label case* follows a similar trend to that of the original label configuration; however, due to the elevated emissivity, the final temperature was further reduced. Nonetheless, this temperature remains higher than that observed in the polymer case configuration. This indicates that the additional volume,

due to the high heat capacity of PLA, is capable of absorbing a significant amount of thermal energy, thereby contributing to further cooling of the cell before transferring heat to the environment.

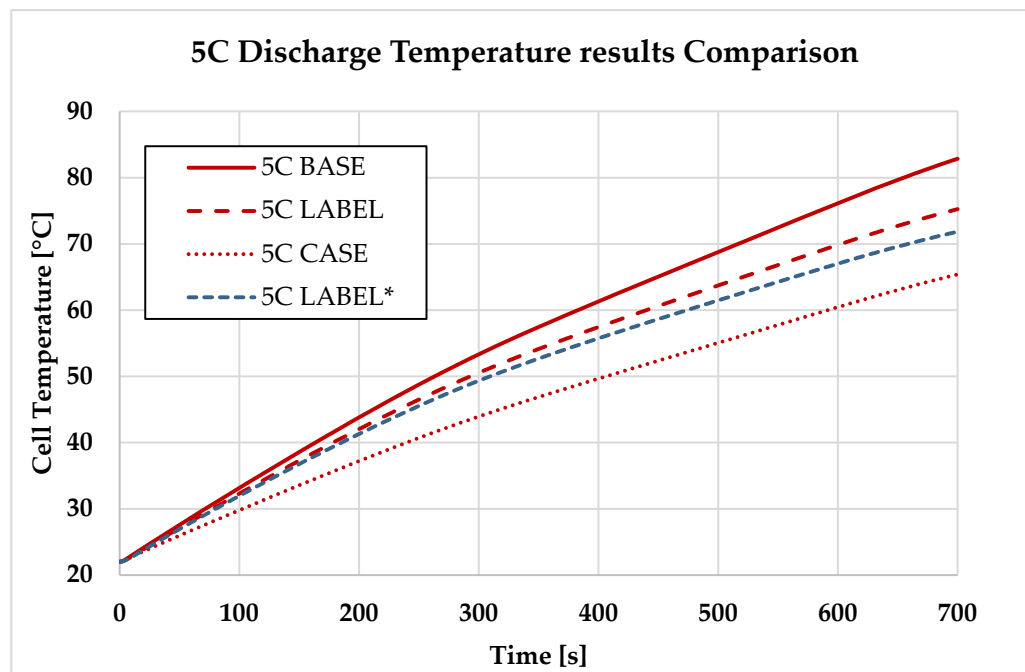


Figure 18. Temperature comparison at $5\times C$ discharge of all three cases and an extra label* case with $\epsilon \approx 0.95$ surface emissivity.

3.6. Physical Testing and Validation

Based on the simulation results, laboratory experiments were conducted to test the applicability of enhanced radiative heat transfer. However, physical experiments were limited to $1\times C$, $2\times C$, and $3\times C$ discharge rates. This limitation was necessary because, as demonstrated by the physical tests on the base case, the battery cell would reach the softening temperature of the available 3D-printable PLA filament under $4\times C$ and $5\times C$ discharge conditions. For safety and experimental repeatability, this practical constraint had to be observed. Nevertheless, the simulation results at these higher discharge rates already predicted significant thermal performance gains, which appear to be confirmed and even slightly exceeded by the physical test results. As shown in Figure 19, the highest discharge experiment at $3\times C$ reveals a notable temperature difference between the base case and the 3D-printed polymer case. In the final discharge phase, the proposed configuration demonstrates an improvement exceeding $12\text{ }^{\circ}\text{C}$. Furthermore, similar to the simulation results, the curve for the polymer case approaches a more linear trend, whereas the Base case exhibits a more dynamic thermal behavior.

The physical experiments yielded results that were, on average, $2.5\text{ }^{\circ}\text{C}$ better than those predicted by the simulations, as illustrated in Figure 20, which compares simulated and empirical outcomes. Despite this difference, the overall trend remains consistent across most discharge processes. The most notable divergence in slope occurs within the first 100 s, corresponding approximately to the SOC 100–90% range, as well as in the final phase between 1000 and 1100 s, corresponding to the SOC 10–0% interval. These deviations highlight the simplifications made during the modeling process.

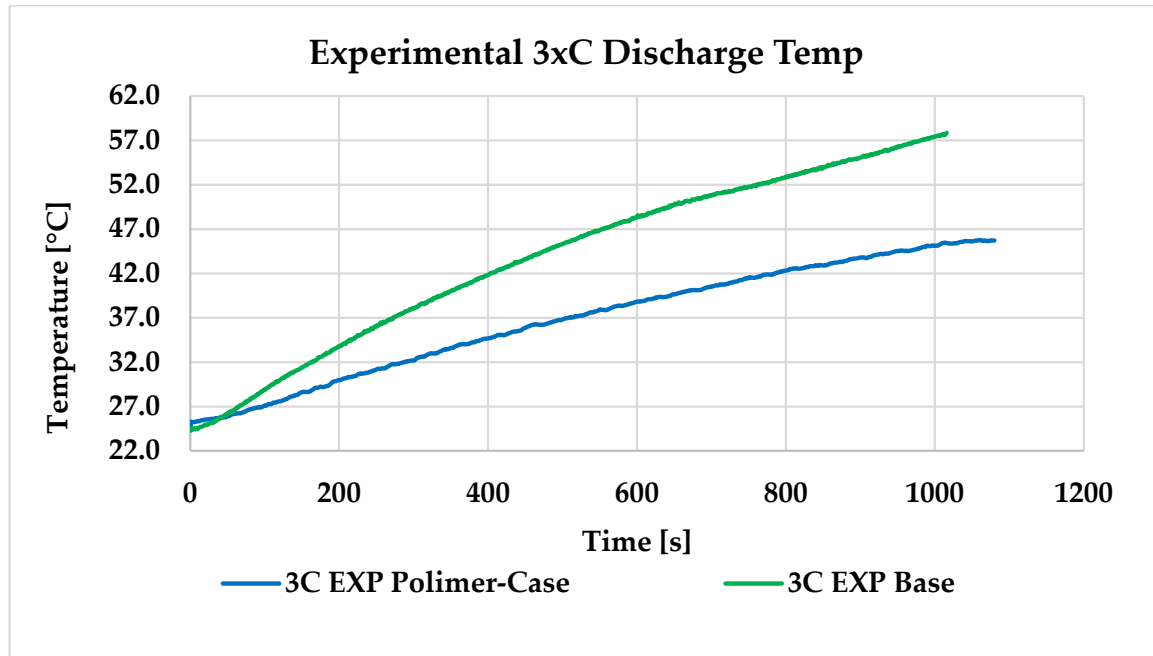


Figure 19. Temperature results at $3\times C$ discharge level of experimental base and experimental polymer case.

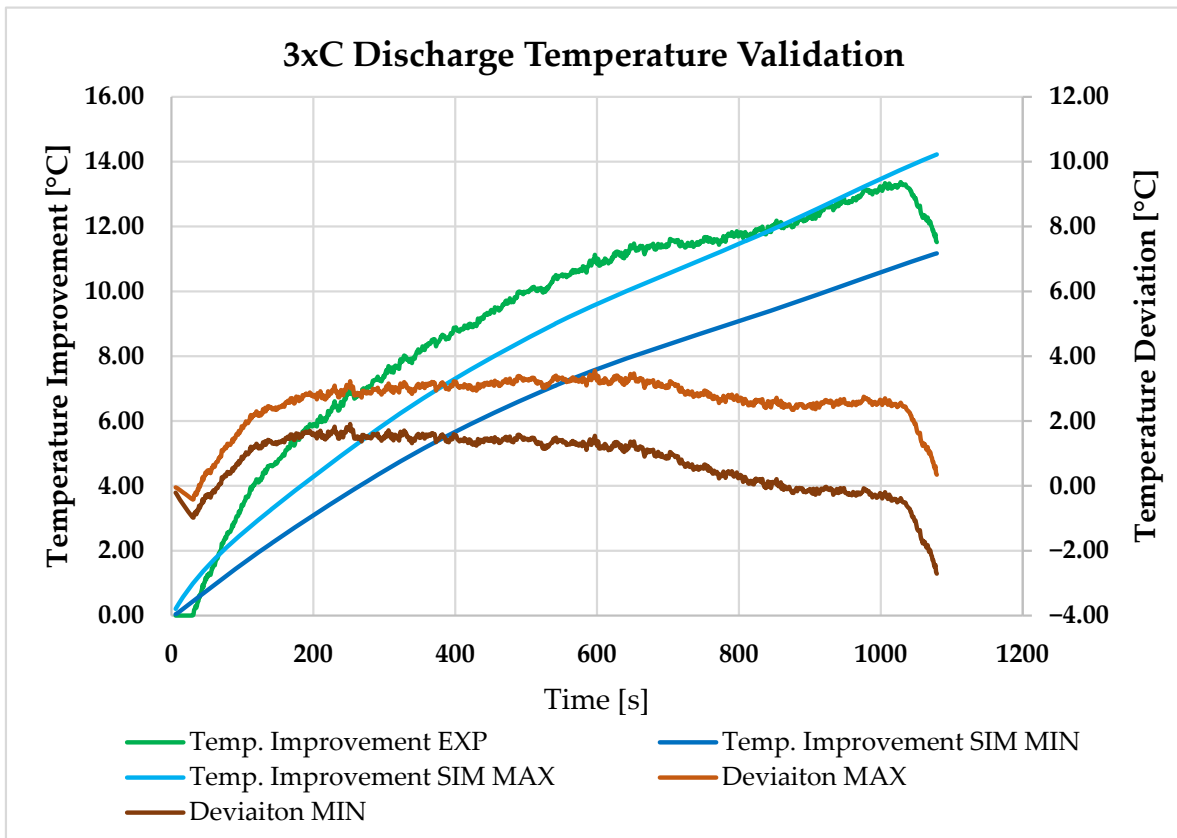


Figure 20. Comparison of experimental and simulation regarding temperature gained during discharge and the average deviation between them.

The theoretical OCV curves applied may be inaccurate at the initial and final states, which are fundamental inputs for determining the heat generation curve used in the simulations (Equation (10)).

During the optimization of the CFD model, several input parameters were varied to evaluate their impact on the simulation outcomes. The influence of these changes proved to be smaller than the deviation observed in the physical measurements.

Upon analyzing the results, it was found that the specific sensor location did not affect the trend of the temperature profiles but influenced the magnitude, introducing a deviation of approximately 2–3 °C. In the case of the polymer case simulation, when the temperature is measured progressively deeper within the PLA layer instead of directly at the cell surface and then toward the external surface, the average deviation gradually decreases down to 0.72 °C. This value falls within the margin of error of the sensor used. Therefore, it appears plausible that, based on the measurement strategy presented, the selected sensor type may not have been the most appropriate choice. (See Figure 20, Deviation MIN and Deviation MAX.)

Another possible explanation is that the PLA material used for the case may begin to soften even at relatively low temperatures, potentially enabling additional heat absorption. This behavior could account for the improved thermal performance observed in the measurements compared to the simulation results.

Lastly, the average temperature improvement observed may also be attributed to geometrical deviations arising from surface waviness caused by the layer structure inherent to the 3D printing process, an effect not accounted for in the simulation. The schematic illustration shown in Figure 21 represents the surface structure resulting from the layer-wise build-up and the orientation of radiative heat flux from the geometry toward the environment. This layered construction slightly increases the surface area and produces a favorable view factor for radiative heat transfer from the battery cell within the side walls of the test chamber. Accurately modeling such surface characteristics in a numerical environment would require a highly refined surface mesh. Due to the associated increase in computational cost, a precise geometric representation of the surface was omitted. As a result, the mesh remained significantly more robust, and the solution could be obtained substantially faster.

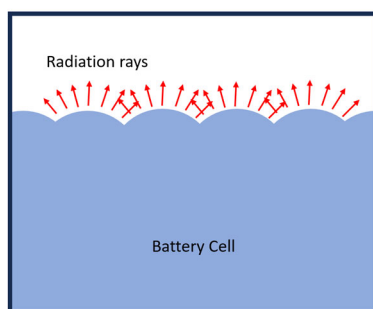


Figure 21. Schematic view of the 3D printed surface of the polymer case.

4. Conclusions

The simulation cases based on physical tests and laboratory experiments demonstrated that increasing surface emissivity can enhance the heat dissipation of battery cells toward the environment. The proposed solution (polymer case) further improved radiative heat transfer. The results showed that enhanced radiative dissipation can improve the order of magnitude at high discharge rates, even at room temperature. Under 5×C discharge, the high-emissivity enclosure reached nearly the same temperature as the non-optimized base case at 4×C. Moreover, when examined as a function of time, the proposed solution significantly extended the thermal response time of the system. This was confirmed by physical testing; at a 3×C load, it took 400 s longer for the polymer case to reach the same temperature level (+40 °C) compared to the base case.

The polymer material and chosen wall thickness also present future research opportunities for application at the module level, facilitating heat transfer from multiple cells to the environment. It is important to note, however, that both the measurement and simulation environments were designed to allow for radiative heat transfer, thus supporting the effectiveness of the proposed solution. Factors such as wall-to-wall distances and favorable view factors are critical for this mode of heat transfer to be effective. These parameters and their variations were not investigated in this study. Additionally, the wall thickness of the tested polymer enclosure was considered a constant. However, the spacing between boundary surfaces, the thermal properties of the polymer, and its wall thickness represent further optimization opportunities.

It is also worth emphasizing that the 3D printing technology used offers various other possibilities for optimizing conductive heat transfer. This includes the application of additives, differences in layer orientation, or the custom geometry of the external surfaces in contact with air, each of which could be leveraged to optimize thermal dissipation.

Although the presented simulation method could be further optimized, it offers a fast and cost-effective approach to battery discharge testing, reproducing trends that align with empirical results. As such, it supports the development of thermal management systems for batteries. Based on physical measurements, the input parameters ensure the necessary accuracy, which can be further improved by using detailed OCV curve data and high-resolution sampling of surface temperatures.

Author Contributions: Conceptualization, G.K., S.K.S., and S.F.; methodology, G.K., S.K.S., and S.F.; software, G.K., S.K.S., and S.F.; validation, G.K., S.K.S., and S.F.; formal analysis, G.K., S.K.S., and S.F.; investigation, G.K., S.K.S., and S.F.; resources, G.K., S.K.S., and S.F.; data curation, G.K., S.K.S., and S.F.; writing—original draft preparation, G.K., S.K.S., and S.F.; writing—review and editing, G.K., S.K.S., and S.F.; visualization, G.K., S.K.S., and S.F.; supervision, G.K., S.K.S., and S.F.; project administration, G.K., S.K.S., and S.F.; funding acquisition, G.K., S.K.S., and S.F. All authors have read and agreed to the published version of the manuscript.

Funding: This research received no external funding.

Data Availability Statement: All of the data are within the paper.

Acknowledgments: Supported by the EKÖP-24-4-II-SZE-61 University Research Scholarship Program of the Ministry for Culture and Innovation from the source of the National Research, Development and Innovation Fund.

Conflicts of Interest: The authors declare no conflicts of interest.

Abbreviations

| | |
|------|---|
| BTM | Battery Thermal Management |
| CFD | Computational Fluid Dynamics |
| EV | Electric Vehicle |
| FDOM | Finite Volume Discrete Ordinates Method |
| IHTA | Inverse Heat Transfer Analysis |
| OCV | Open Circuit Voltage |
| PCM | Phase Change Material |
| PLA | Phase Change Material |
| S2S | Surface to Surface |
| SOC | State of Charge |
| UAS | Unmanned Aerial System |

References

- Waldmann, T.; Scurtu, R.G.; Richter, K.; Wohlfahrt-Mehrens, M. 18650 vs. 21700 Li-Ion Cells—A Direct Comparison of Electrochemical, Thermal, and Geometrical Properties. *J. Power Sources* **2020**, *472*, 228614. [[CrossRef](#)]
- Quinn, J.B.; Waldmann, T.; Richter, K.; Kasper, M.; Wohlfahrt-Mehrens, M. Energy Density of Cylindrical Li-Ion Cells: A Comparison of Commercial 18650 to the 21700 Cells. *J. Electrochem. Soc.* **2018**, *165*, A3284–A3291. [[CrossRef](#)]
- Ohneseit, S.; Finster, P.; Floras, C.; Lubenau, N.; Uhlmann, N.; Seifert, H.J.; Ziebert, C. Thermal and Mechanical Safety Assessment of Type 21700 Lithium-Ion Batteries with NMC, NCA and LFP Cathodes—Investigation of Cell Abuse by Means of Accelerating Rate Calorimetry (ARC). *Batteries* **2023**, *9*, 237. [[CrossRef](#)]
- Saxon, A.; Yang, C.; Santhanagopalan, S.; Keyser, M.; Colclasure, A. Li-Ion Battery Thermal Characterization for Thermal Management Design. *Batteries* **2024**, *10*, 136. [[CrossRef](#)]
- Samsung SDI Co., Ltd. INR21700-50S Lithium-Ion Rechargeable Cell Specification; Version 0.2; Samsung SDI: Yongin-si, Republic of Korea, 2020. Available online: <https://www.dnkpower.com/wp-content/uploads/2022/07/SAMSUNG-INR21700-50S-Cell-Specification.pdf> (accessed on 17 June 2025).
- Buidin, T.I.C.; Mariasiu, F. Battery Thermal Management Systems: Current Status and Design Approach of Cooling Technologies. *Energies* **2021**, *14*, 4879. [[CrossRef](#)]
- Li, J.; Zhu, Z. Battery Thermal Management Systems of Electric Vehicles Space for Picture. Master’s Thesis, Division of Vehicle Engineering & Autonomous Systems, Road Vehicle Aerodynamics and Thermal Management, Chalmers University of Technology, Göteborg, Sweden, 2014.
- Shadman Rad, M.; Danilov, D.L.; Baghalha, M.; Kazemeini, M.; Notten, P.H.L. Adaptive Thermal Modeling of Li-Ion Batteries. *Electrochim. Acta* **2013**, *102*, 183–195. [[CrossRef](#)]
- Sheng, L.; Zhang, Z.; Su, L.; Zhang, H.; Zhang, H.; Li, K.; Fang, Y.; Ye, W. A Calibration Calorimetry Method to Investigate the Thermal Characteristics of a Cylindrical Lithium-Ion Battery. *Int. J. Therm. Sci.* **2021**, *165*, 106891. [[CrossRef](#)]
- Hwang, F.S.; Confrey, T.; Scully, S.; Callaghan, D.; Nolan, C.; Kent, N.; Flannery, B. Modelling of Heat Generation in an 18650 Lithium-Ion Battery Cell under Varying Discharge Rates. In Proceedings of the 5th Thermal and Fluids Engineering Summer Conference, New Orleans, LA, USA, 5–8 April 2020; Begell House Inc.: Danbury, CT, USA, 2020; Volume 2020, pp. 333–341.
- Tan, Y.; Li, Y.; Gu, Y.; Liu, W.; Fang, J.; Pan, C. Numerical Study on Heat Generation Characteristics of Charge and Discharge Cycle of the Lithium-Ion Battery. *Energies* **2024**, *17*, 178. [[CrossRef](#)]
- Tan, Z.M.; Liu, J.Y.; Li, Q. Importance of Heat Transfer by Radiation in Li-Ion Batteries during Thermal Abuse. *Electrochem. Solid-State Lett.* **2000**, *3*, 305–308.
- Gümüşsü, E.; Ekici, Ö.; Köksal, M. 3-D CFD Modeling and Experimental Testing of Thermal Behavior of a Li-Ion Battery. *Appl. Therm. Eng.* **2017**, *120*, 484–495. [[CrossRef](#)]
- Liu, J.; Chavan, S.; Kim, S.C. Investigation of the Electrochemical and Thermal Characteristics of NCM811-21700 Cylindrical Lithium-Ion Battery: A Numerical Study and Model Validation. *Energies* **2023**, *16*, 6407. [[CrossRef](#)]
- Madani, S. Experimental Study of the Heat Generation of a Lithium-Ion Battery. *ECS Trans.* **2020**, *99*, 419–428. [[CrossRef](#)]
- Huang, R.; Xu, Y.; Wu, Q.; Chen, J.; Chen, F.; Yu, X. Simulation Study on Heat Generation Characteristics of Lithium-Ion Battery Aging Process. *Electronics* **2023**, *12*, 1444. [[CrossRef](#)]
- Du, J.; Tao, H.; Chen, Y.; Yuan, X.; Lian, C.; Liu, H. Thermal Management of Air-Cooling Lithium-Ion Battery Pack. *Chin. Phys. Lett.* **2021**, *38*, 118201. [[CrossRef](#)]
- Liu, H.; Yang, K.; Gao, F.; Chen, H.; Hui, D.; Zhang, H. The Thermal Simulation Research of Lithium Ion Battery Pack. *Destech Trans. Eng. Technol. Res.* **2017**, mdm. [[CrossRef](#)]
- Lee, G. Lectro-Thermal Analysis of a Pouch-Type Lithium-Ion Battery with a High Discharge Rate for Urban Air Mobility. *Batteries* **2023**, *9*, 476. [[CrossRef](#)]
- Madani, S.; Schaltz, E.; Kær, S.K. Thermal Simulation of Phase Change Material for Cooling of a Lithium-Ion Battery Pack. *Electrochim* **2020**, *1*, 439–449. [[CrossRef](#)]
- Madani, S. Analysis of a Phase Change Material for Thermal Management of a Lithium-Ion Battery. *ECS Trans.* **2020**, *99*, 411–418. [[CrossRef](#)]
- Zhao, R.; Liu, J.; Ma, F. A Comprehensive Comparison of the Phase Change Material-Based Internal and External Cooling Systems. *ECS Trans.* **2020**, *97*, 195. [[CrossRef](#)]
- Chen, H.; Buston, J.; Gill, J.; Howard, D.; Williams, R.; Read, E. A Simplified Mathematical Model for Heating-Induced Thermal Runaway of Lithium-Ion Batteries. *J. Electrochem. Soc.* **2021**, *168*, 010502. [[CrossRef](#)]
- Madani, S.; Ziebert, C.; Marzband, M. Thermal Behavior Modeling of Lithium-Ion Batteries: A Comprehensive Review. *Symmetry* **2023**, *15*, 1597. [[CrossRef](#)]
- Wang, Z.; Ma, J.; Zhang, L. Finite Element Thermal Model and Simulation for a Cylindrical Li-Ion Battery. *IEEE Access* **2017**, *5*, 15372–15379. [[CrossRef](#)]
- Balmer, R. *Modern Engineering Thermodynamics*; Academic Press: Cambridge, MA, USA, 2011.

27. Moukalled, F.; Mangani, L.; Darwish, M. *Fluid Mechanics and Its Applications The Finite Volume Method in Computational Fluid Dynamics*; Springer International Publishing: Cham, Switzerland, 2016; Volume 113, ISBN 978-3-319-16873-9/978-3-319-16874-6.
28. Versteeg, H.K.; Malalasekera, W. *An Introduction to Computational Fluid Dynamics*, 2nd ed.; Pearson Education Limited: Harlow, UK, 2007; Volume 2, ISBN 978-0-13-127498-3.
29. Welahettige, P.; Vaagsaether, K. Comparison of OpenFOAM and ANSYS Fluent. In Proceedings of the 9th EUROSIM Congress on Modelling and Simulation (EUROSIM 2016) and the 57th SIMS Conference on Simulation and Modelling (SIMS 2016), Oulu, Finland, 13–15 September 2016; Linköping University Electronic Press: Linköping, Sweden, 2016; Volume 142, pp. 1005–1012.
30. Zou, Y.; Zhao, X.; Chen, Q. Comparison of STAR-CCM+ and ANSYS Fluent for Simulating Indoor Airflows. *Build. Simul.* **2017**, *11*, 165–174. [[CrossRef](#)]
31. ANSYS, Inc. *ANSYS Fluent Theory Guide*; ANSYS, Inc.: Canonsburg, PA, USA, 2021; pp. 167–206.
32. Shelke, A.V.; Buston, J.E.H.; Gill, J.; Howard, D.; Williams, R.C.E.; Read, E.; Abaza, A.; Cooper, B.; Richards, P.; Wen, J.X. Combined Numerical and Experimental Studies of 21700 Lithium-Ion Battery Thermal Runaway Induced by Different Thermal Abuse. *Int. J. Heat. Mass. Transf.* **2022**, *194*, 123099. [[CrossRef](#)]
33. Verdério Júnior, S.A.; Scalon, V.L.; Avallone, E.; Mioralli, P.C. Numerical Validation of Viewfactor and FVDOM Radiation Models of Openfoam® and Application in the Study of Food Furnaces. *Ingeniare* **2018**, *26*, 546–556. [[CrossRef](#)]
34. Cao, R.; Zhang, X.; Yang, H. Prediction of the Heat Generation Rate of Lithium-Ion Batteries Based on Three Machine Learning Algorithms. *Batteries* **2023**, *9*, 165. [[CrossRef](#)]
35. Barai, A.; Widanage, W.D.; Marco, J.; McGordon, A.; Jennings, P. A Study of the Open Circuit Voltage Characterization Technique and Hysteresis Assessment of Lithium-Ion Cells. *J. Power Sources* **2015**, *295*, 99–107. [[CrossRef](#)]
36. Birk, C.R.; McTurk, E.; Roberts, M.R.; Bruce, P.G.; Howey, D.A. A Parametric Open Circuit Voltage Model for Lithium Ion Batteries. *J. Electrochem. Soc.* **2015**, *162*, A2271–A2280. [[CrossRef](#)]
37. Lei, H.; Han, Y.Y. The Measurement and Analysis for Open Circuit Voltage of Lithium-Ion Battery. *J. Phys. Conf. Ser.* **2019**, *1325*, 012173. [[CrossRef](#)]
38. Sarmadian, A.; Yu, Y.; Marco, J.; Shollock, B.; Restuccia, F. An Experimentally-Verified Thermal-Electrochemical Simulation Model of a 21700 Cell Using a Lumped Semi-Empirical Battery Model. In Proceedings of the 16th International Conference on Heat Transfer, Fluid Mechanics and Thermodynamics (HEFAT2022), Amsterdam, The Netherlands, 8–10 August 2022; pp. 128–133.
39. Baccouche, I.; Jemmali, S.; Manai, B.; Omar, N.; Essoukri Ben Amara, N. Improved OCV Model of a Li-Ion NMC Battery for Online SOC Estimation Using the Extended Kalman Filter. *Energies* **2017**, *10*, 764. [[CrossRef](#)]
40. Baccouche, I.; Essoukri, N.; Amara, B.; Jemmali, S.; Mlayah, A.; Manai, B. Implementation of an Improved Coulomb-Counting Algorithm Based on a Piecewise SOC-OCV Relationship for SOC Estimation of Li-Ion Battery Implementation of an Improved Coulomb-Counting Algorithm Based on a Piecewise SOC-OCV Relationship for SOC Estimation of Li-Ion Battery. *arXiv* **2018**, arXiv:1803.10654. [[CrossRef](#)]
41. Yu, Q.Q.; Xiong, R.; Wang, L.Y.; Lin, C. A Comparative Study on Open Circuit Voltage Models for Lithium-Ion Batteries. *Chin. J. Mech. Eng. (Engl. Ed.)* **2018**, *31*, 65. [[CrossRef](#)]
42. Sundaresan, S.; Devabattini, B.C.; Kumar, P.; Pattipati, K.R.; Balasingam, B. Tabular Open Circuit Voltage Modelling of Li-Ion Batteries for Robust SOC Estimation. *Energies* **2022**, *15*, 9142. [[CrossRef](#)]
43. Han, U.; Choi, H.; Lee, H.; Lee, H. Inverse Heat Transfer Analysis Method to Determine the Entropic Coefficient of Reversible Heat in Lithium-Ion Battery. *Int. J. Energy Res.* **2023**, *2023*, 9929496. [[CrossRef](#)]
44. Wen, C.D.; Mudawar, I. Modeling the Effects of Surface Roughness on the Emissivity of Aluminum Alloys. *Int. J. Heat. Mass. Transf.* **2006**, *49*, 4279–4289. [[CrossRef](#)]
45. Yu, H.; Zhang, H.; Shi, J.; Liu, S.; Yi, Z.; Xu, S.; Wang, X. Thermal Parameters of Cylindrical Power Batteries: Quasi-Steady State Heat Guarding Measurement and Thermal Management Strategies. *Appl. Therm. Eng.* **2023**, *231*, 120959. [[CrossRef](#)]
46. Wang, C.L.; Leong, J.C. Analysis of Thermal Management Strategies for 21700 Lithium-Ion Batteries Incorporating Phase Change Materials and Porous Copper Foam with Different Battery Orientations. *Energies* **2024**, *17*, 1553. [[CrossRef](#)]
47. Liu, G.; Ouyang, M.; Lu, L.; Li, J.; Han, X. Analysis of the Heat Generation of Lithium-Ion Battery during Charging and Discharging Considering Different Influencing Factors. *J. Therm. Anal. Calorim.* **2014**, *116*, 1001–1010. [[CrossRef](#)]
48. Lin, C.; Wen, H.; Liu, L.; Liu, S.; Ma, T.; Fan, B.; Wang, F. Heat Generation Quantification of High-Specific-Energy 21700 Battery Cell Using Average and Variable Specific Heat Capacities. *Appl. Therm. Eng.* **2021**, *184*, 116215. [[CrossRef](#)]

Disclaimer/Publisher’s Note: The statements, opinions and data contained in all publications are solely those of the individual author(s) and contributor(s) and not of MDPI and/or the editor(s). MDPI and/or the editor(s) disclaim responsibility for any injury to people or property resulting from any ideas, methods, instructions or products referred to in the content.